



## 12MW Horns Rev experiment

**Hasager, Charlotte Bay; Peña, A.; Mikkelsen, Torben; Courtney, Michael S; Antoniou, Ioannis; Gryning, Sven-Erik; Hansen, Per; Sørensen, P.B.**

*Publication date:*  
2007

*Document Version*  
Publisher's PDF, also known as Version of record

[Link back to DTU Orbit](#)

*Citation (APA):*  
Hasager, C. B., Peña, A., Mikkelsen, T., Courtney, M. S., Antoniou, I., Gryning, S-E., Hansen, P., & Sørensen, P. B. (2007). *12MW Horns Rev experiment*. Risø National Laboratory. Denmark. Forskningscenter Risoe. Risoe-R No. 1506(EN)

---

### General rights

Copyright and moral rights for the publications made accessible in the public portal are retained by the authors and/or other copyright owners and it is a condition of accessing publications that users recognise and abide by the legal requirements associated with these rights.

- Users may download and print one copy of any publication from the public portal for the purpose of private study or research.
- You may not further distribute the material or use it for any profit-making activity or commercial gain
- You may freely distribute the URL identifying the publication in the public portal

If you believe that this document breaches copyright please contact us providing details, and we will remove access to the work immediately and investigate your claim.

## 12MW Horns Rev Experiment

C. B. Hasager, A. Peña, T. Mikkelsen, M. Courtney, I. Antoniou, S.-E. Gryning, P. Hansen (Risø) and P. B. Sørensen (DONG energy)

Risø-R-1506(EN)



**Author:** C. B. Hasager, A. Peña, T. Mikkelsen, M. Courtney, I. Antoniou, S.-E. Gryning, P. Hansen (Risø) and P. B. Sørensen (DONG energy)  
**Title:** 12MW Horns Rev Experiment  
**Department:** Wind Energy

**Abstract (max. 2000 char.):**

The 12MW project with the full title '12 MW wind turbines: the scientific basis for their operation at 70 to 270 m height offshore' has the goal to experimentally investigate the wind and turbulence characteristics between 70 and 270 m above sea level and thereby establish the scientific basis relevant for the next generation of huge 12 MW wind turbines operating offshore. The report describes the experimental campaign at the Horns Rev offshore wind farm at which observations from Doppler Laser LIDAR and SODAR were collected from 3 May to 24 October 2006. The challenges for mounting and operating the instruments on the transformer platform at Horns Rev were overcome by a close collaboration between DONG energy and Risø National Laboratory DTU.

The site is presented. In particular, three tall offshore meteorological masts, up to 70 m tall, provided a useful source of meteorological data for comparison to the remotely sensed wind and turbulence observations. The comparison showed high correlation. The LIDAR and SODAR wind and turbulence observations were collected far beyond the height of the masts (up to 160 m above sea level) and the extended profiles were compared to the logarithmic wind profile. Further studies on this part of the work are on-going. Technical detail on LIDAR and SODAR are provided as well as theoretical work on turbulence and atmospheric boundary layer flow. Selected results from the experimental campaign are reported.

**Risø-R-1506(EN)**  
**October 2007**

**ISSN 0106-2840**  
**ISBN 87-550-3418-7**

**Contract no.:**  
Sagsnr. 2104-05-0013

**Group's own reg. no.:**  
1130314-01

**Sponsorship:**  
The Danish Council for Strategic Research

**Cover :**  
Sketch of potential remote sensing observations at an offshore wind farm.

**Pages: 84**  
**Tables: 5**  
**References: 46**

Information Service Department  
Risø National Laboratory  
Technical University of Denmark  
P.O.Box 49  
DK-4000 Roskilde  
Denmark  
Telephone +45 46774004  
[bibl@risoe.dk](mailto:bibl@risoe.dk)  
Fax +45 46774013  
[www.risoe.dk](http://www.risoe.dk)

# Contents

## **Preface 5**

## **1 Introduction on the 12MW project 6**

- 1.1 Background 6
- 1.2 Goal 7
  - 1.2.1 Innovation 7
  - 1.2.2 Objective 7
- 1.3 Theoretical basis 7
- 1.4 Technical basis 8
- 1.5 Scientific issues and state of the art 8
- 1.6 Methodology 9
- 1.7 Report structure 9

## **2 The 12MW Horns Rev experiment 10**

- 2.1 Site description 11
  - 2.1.1 The wind farm 11
  - 2.1.2 Meteorological masts 13
  - 2.1.3 Wind conditions 16
- 2.2 Meteorological observations (up to 70 m) 17
  - 2.2.1 Mast distortion 18
  - 2.2.2 Observed mean wind speed 22
  - 2.2.3 Mean wind speed profiles 23

## **3 The ZephIR LiDAR profiler (up to 160 m) 25**

- 3.1 The ZephIR LiDAR – theory of operation 25
- 3.2 Measurement imperfections 28
- 3.3 Experimental setup and system operation 29
- 3.4 Data management and processing 30

## **4 Theory on LIDAR and turbulence 32**

- 4.1 The ZephIR LIDAR's Spatial Measurement Volume 32
- 4.2 Turbulence seen by the QinetiQ ZephIR LiDAR: 35
  - 4.2.1 The Effects of Conical scanning and Lorentzian Probe 35
  - 4.2.2 Modelling the ZephIR's spatial filters due to averaging 37
- 4.3 The Effect on ZephIR LiDAR measurements: 39
  - 4.3.1 Conclusion on measured turbulence level 41
- 4.4 The filter effects on the ZephIR measured "TQE" 41

## **5 A generic description of the SODAR instrument (up to 300 m) 45**

- 5.1 SoDAR calibration principles 48

## **6 Mixing layer height theory 49**

- 6.1 Boundary layer over the sea 49
- 6.2 Measurements of the boundary layer height 49
- 6.3 Marine boundary layer in the coastal zone. 50
- 6.4 The height of the marine boundary layer at open sea 55
- 6.5 Conclusions for mixing layer height theory 57
  - 6.5.1 Coastal marine boundary layers 57
  - 6.5.2 Open sea boundary layers 58

## **7 Results 59**

7.1 Comparison results 61

7.1.1 Mean wind speed 61

7.1.2 Turbulence 64

7.2 Wind and turbulence profiles 68

7.2.1 Modelling the offshore wind 70

7.2.2 The sea roughness length 72

7.2.3 Charnock's wind profiles 74

7.2.4 Turbulence profiles 76

## **8 Summary 78**

## **9 Conclusion and future work 79**

## **Acknowledgements 79**

## **References 80**

## **Appendix I 83**

## **Preface**

The project '12 MW wind turbines: the scientific basis for their operation at 70 to 270 m height offshore' is supported financially by The Danish Council for Strategic Research during the year 2006 to 2009.

The present report describes the Horns Rev experimental work, data collection and preliminary results. The experiment was done in close collaboration between DONG energy and Risø National Laboratory from 3 May to 24 October 2006.

# 1 Introduction on the 12MW project

The project ‘12 MW wind turbines: the scientific basis for their operation at 70 to 270 m height offshore’ is funded by the the Danish Council for Strategic Research during the year 2006 to 2009. The project is called ‘12MW’. In the first year an experiment was carried out at Horns Rev. This is described in the present report. The partners Risø DTU and DONG energy cooperates closely in the project.

## 1.1 Background

Wind turbine dimensions have evolved rapidly (see Fig. 1.1). Thus the height in the atmospheric boundary layer of wind turbine operation is increasing (table 1.1). At Høvsøre Test Station, Risø ([http://www.risoe.dk/rispubl/Risnyt/risnytpdf/ris0300/riso-3-2000s4\\_5.pdf](http://www.risoe.dk/rispubl/Risnyt/risnytpdf/ris0300/riso-3-2000s4_5.pdf)) turbines up to 8 MW can be tested but even larger turbines are in preparation up to 12 MW (de Vries, E, 2005). This development puts a strong demand on our understanding of the atmospheric flow and turbulence characteristics at very high heights.

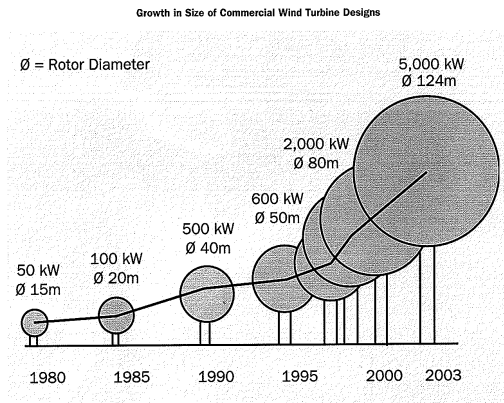


Figure 1.1 Dimensions of wind turbines through time.

Table 1.1 Dimensions of multi-MW wind turbines.

Turbine	Hub-height	Rotor diameter	Lower tip	Upper tip
2 MW	70 m	80 m	30 m	110 m
5 MW	110 m	124 m	48 m	172 m
8 MW	140 m	160 m	60 m	220 m
12 MW	170 m	190 m	75 m	265 m

Small turbines operate in the lower part of the atmospheric boundary layer. Here the logarithmic wind profile is valid and turbulence statistics are well known. Meteorological data at Horns Rev offshore wind farm from DONG energy (<http://test7.scancommerce.dk/hornsrev/>) supports this (Sørensen, 2005a, 2005b; Jensen et al. 2004, Sommer, 2003). Offshore data also verify that thermal stratification (Pryor and Barthelmie, 2002, Barthelmie 1999) and sea surface roughness (Barthelmie, 2001, Lange et al. 2004) are key-issues in coastal marine wind systems studied so far up to 70 m. At higher levels winds are largely unknown due to severe practical offshore measurement difficulties.

The challenge is therefore to improve our knowledge on offshore wind and turbulence characteristics for the next generation of multi-MW wind turbines that will come to operate at heights ranging from 70 to 270 m above sea level.

It is suggested to improve offshore winds and turbulence prediction capabilities at these heights based on available new and proven remote sensing equipment, wind and turbulence quantification, and modeling.

The strategic aim is to supply Danish wind industry relevant results.

## 1.2 Goal

The goal of the project is to experimentally investigate the wind and turbulence characteristics between 70 and 270 m above sea level and thereby establish the scientific basis relevant for the next generation of huge 12 MW wind turbines operating offshore. This will be done using state of the art wind remote sensing measurement techniques for data collection at an offshore wind farm site in Denmark.

### 1.2.1 Innovation

The innovations are establishment of new reference data and new wind and turbulence profiles at 70 to 270 m, unique experimental set-up at offshore wind farm in rough environment, advanced signal processing of state of the art remote sensing wind observations and estimating the mixing layer height from remote sensing observations.

### 1.2.2 Objective

To establish new wind and turbulence design models for the next generation of 12 MW turbines operating in the offshore marine environment from 70 to 270 m's height. The design models will be evaluated from observations from Doppler Laser LIDAR, SODAR, backscatter aerosol LIDAR, radiosonde and ceilometer.

## 1.3 Theoretical basis

At high levels offshore - from 70 to 270 m - only very few observations of marine winds are available. These show, however, a variety of features that potentially could jeopardize operation of huge wind turbines, such as:

- increase of the wind speed compared to predictions made by the standard logarithmic profile (Antoniou, 2004a),
- low-level jets with very high winds in stable stratification (Smedman et al., 1995, 2004),
- shallow marine boundary layers with large jumps in wind and direction (Kaimal and Finnigan, 1994),
- extrapolation of the lateral and longitudinal coherent turbulence structures as measured at 78 meters height by Risø for the Great Belt Bridge Consortium predicting coherence at 200 meters height that could interfere destructively with ~200 m huge rotor plans.

To date, standard models for surface layer wind profiles, e.g. the simple logarithmic wind profile ( $dU/dz$ ), is "scaled" by friction velocity ( $u_*$ ) only. This concept, however, *does not* apply above the surface layer. At ~100 meter and above scaling of wind profiles invokes in addition the mixing layer height ( $z_i$ ). Therefore, a new extended wind profile, applicable from the surface and well into the mixing layer

200- 300 meters aloft has been proposed from Høvsøre coastal data up to 168 m height (Gryning *et al.* 2007). Consequently, offshore measurements of  $z_i$  are required.

A model for turbulence profiles from the surface boundary layer up to the mixing height has successfully been tested over land (Gryning *et al.*, 1987) and for urban area (Batchvarova & Gryning 2006) but not yet in the marine environment. Accurate turbulence profiles are of importance for the calculation of wind loads on structures (wind turbines).

#### 1.4 Technical basis

To measure winds and turbulence between 70 and 270 m is a true challenge. A conventional meteorological mast for these heights over sea is utterly expensive. Remote sensing technologies have consequently become an attractive option, given their data are scientifically interpreted. New remote sensing technologies such as Doppler Laser LIDAR and SODAR for accurate wind observations at high levels have become available. Advantages of these instruments are that they, at reasonable cost, observe winds and turbulence up to 300 m from their local position. Successful operation of SODAR (Barthelmie *et al.* 2003) in the marine environment is demonstrated. Doppler Laser LIDAR wind observations from Høvsøre (Antoniou *et al.*, 2004a) exhibit very high quality. Advanced real-time signal processing is needed for both instruments, in order to obtain high-quality wind observations including turbulence. Mixed layer height (an important scaling parameter) will be monitored from backscattering aerosol LiDAR, radiosoundings and ceilometer.

#### 1.5 Scientific issues and state of the art

The major scientific issue is to experimentally evaluate new mathematical models for prediction of the winds and turbulence characteristics at high levels above the sea. This is crucial for obtaining a detailed design-knowledge for the next-generation multi-MW wind turbines. The turbine structures will be enormous and the wind shear between tip of wings significant. Wind climate at hub-height and across the rotor diameter is unknown. To our knowledge, it has not yet been measured anywhere. Verified models are not available.

Wind and turbulence data will be obtained at high levels in the marine boundary layer in this project. The planned experimental set-up will rely on proven state of the art remote sensing technology applied to operation in a harsh environment.

Horns Rev wind farm offers unique opportunities for safe mounting of the instruments and excellent meteorological observations for comparison in the lower part of the atmosphere (20 to 70 m above sea level). A new wind farm (Horns Rev 2) is in the planning phase with likelihood that 4 or 5 MW wind turbines will be erected in the vicinity. In this case, *hub-heights of the new turbines will be ~40 m and tip of wings up to 100 m above current wind observations.*

The '12MW'-project will quantify winds and turbulence offshore at 70 to 270 m height. Such a project requires guidance from a professional experimental research team because it is beyond capabilities of wind turbine manufacturers and wind energy developers to deploy new remote sensing sensors in an experimental campaign, to apply advanced signal processing to the data stream, to retrieve and finally to evaluate theoretical models

on winds and turbulence. The ‘12MW’ project is basis foundation research with strategic aim for the next generation of multi-MW turbines.

## 1.6 Methodology

The two models on marine winds and turbulence high above sea surface are based on the following a set of observed parameters

- wind speed and direction at various levels ( $U(z)$ ,  $dir$ )
- turbulence parameters at various levels ( $u^*$ ,  $\sigma_u$ ,  $\sigma_v$ ,  $\sigma_w$ )
- air temperature at various levels ( $T_a$ )
- heat flux observations at one level ( $H$ )
- mixing layer height ( $z_i$ )

The methodology is to measure the above parameters with the highest possible accuracy for six months offshore at the Horns Rev wind farm. The following instruments will be used for the vertical dimension:

- Three tall meteorological masts with sonic and cup anemometers, thermometers (up to 70 m)
- Doppler Laser LIDAR (up to 160 m),
- SODAR (up to 270 m),
- Ceilometer (up to 3.000 m)
- Aerosol backscatter LIDAR (up to 1.000 m),
- Radiosounding (up to 3.000 m),

## 1.7 Report structure

The report consists of 11 chapters. Chapter 1 introduces the project, chapter 2 the 12MW Horns Rev experiment, the Horns Rev experimental site and the meteorological observations from three offshore masts in brief. Chapter 3 describes the ZephIR lidar profiler in detail and the method of operation during the experiment and the database established from the experiment. Chapter 4 introduces the theory on turbulence and turbulent kinetic energy versus turbulent ‘QinetiQ’ energy observed by the ZephIR lidar. Chapter 5 briefly outlines SoDAR technology for wind observations. The theory for mixing layer height and the new observational technique: ceilometer for this height is presented in chapter 6. Chapter 7 presents and discusses selected results based on observations from cup anemometers on the three masts, SoDAR and LiDAR. In particular, results using LiDAR for profiling to 160 m above sea level and turbulence results at various heights offshore are presented. Chapter 8 summarized the major findings and chapter 9 contains conclusion and future perspectives.

## 2 The 12MW Horns Rev experiment

*Alfredo Peña*

The future optimal operation of 12MW wind turbines requires analysis of the wind and the turbulence conditions at the heights where they are planned to operate, i.e. from the first couple of meters to levels around 250 m from the base of the turbine.

Such turbines will probably be installed at sites where the wind speeds are usually higher and the turbulence levels lower. These conditions are normally found over homogeneous flat terrain or over the sea. The placement of wind turbines and wind farms at offshore locations has another big advantage over the onshore sites: The visual impact is much lower which is crucial for the future of the wind energy.

The Horns Rev experiment consists in the analysis and understanding of the wind conditions of one of the potential areas where these turbines can be installed: The Horns Rev region in the Danish North Sea (see Figure 2.1).

At Horns Rev was installed one of the world's biggest wind farms in terms of installed capacity (160 MW). The wind conditions and the effects of the wind farm wake are continuously studied from meteorological masts placed around the wind farm. These masts perform observations of wind and sea conditions from a level 4 m BMSL (Below Mean Sea Level) up to a level 62/70 m AMSL (Above Mean Sea Level). This range of heights corresponds to approximately a third of the estimated operation heights covered by a 12 MW turbine; thus there is a need to assess the wind resource at higher levels. The masts at Horns Rev are limited in terms of height (and in general all meteorological masts) because it is too expensive to erect higher masts due to the costs and the structural problems.



*Figure 2.1. Horns Rev offshore wind farm. Courtesy of DONG energy.*

The Wind Energy department at Risø is aware of this problem. Therefore, the use of remote sensing instruments has been investigated during recent years. For the experiment at Horns Rev, two ground-based remote sensing instruments, a LiDAR (Light Detection And Ranging) and a SoDAR (Sound Detection And Ranging) were installed on the transformer/platform of the wind farm at 20 m AMSL (see Figure 2.2). This special wind assessment campaign took place during six months from May to October 2006.



*Figure 2.2. Ground-based remote sensing instrumentation on the Horns Rev transformer/platform. To the left: QinetiQ's ZephIR Wind LiDAR. To the right: AQ500 SoDAR.*

The LiDAR unit used was the QinetiQ's ZephIR wind LiDAR which can observe winds and turbulence at five different levels up to around 200 m. The SoDAR is the AQ500 from AQ systems which performs observations of wind and turbulence at different levels and, depending on the configuration mode, the instrument can reach ranges up to 300 m. In this way, the meteorological masts can be used in combination with the observations from the SoDAR and LiDAR to give a scientific base of the wind conditions for the future operation of 12 MW wind turbines.

## **2.1 Site description**

### **2.1.1 The wind farm**

The experiment was performed at the most western point of the coast of Jutland (Blåvandshuk, Esbjerg) in the Danish North Sea (see Figure 2.3). The name of the

region is Horns Rev (in English Horns Reef) due to the prominent form as shown in Figure 2.4.

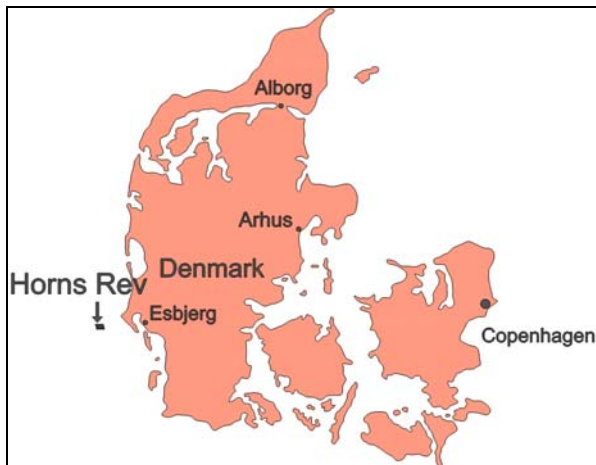


Figure 2.3. Map of Denmark with the location of Esbjerg and Horns Rev at the west coast of Jutland.

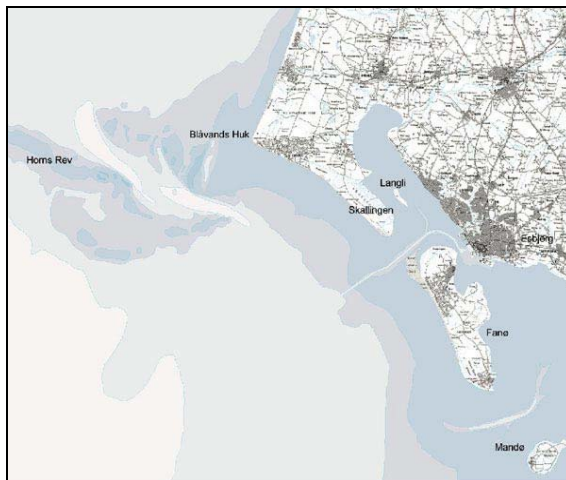


Figure 2.4. The Horns Rev site in the Danish North Sea. Courtesy of DONG energy.

The world's largest offshore wind farm was constructed at Horns Rev in 2002. The wind farm is located at around 12-17 km west from Blåvanshuk (its closest distance to land). The wind park represents the first phase of the plan that the Danish government developed to expand the utilization of non-polluting energy. A total power capacity of 4000 MW should be reached by the year 2030 in Danish waters using energy extracted from wind turbines.

During the summer of 2006, the company Vattenfall obtained 60% ownership of the wind farm, previously operated and maintained by Elsam Engineering A/S. The remaining 40% is now owned by DONG energy.

The wind farm consists of 80 wind turbines forming an oblique rectangle layout of 5x3.8 km (8 horizontal and 10 vertical rows) as it is shown in Figure 2.5. The distance between turbines is 560 m in both directions.

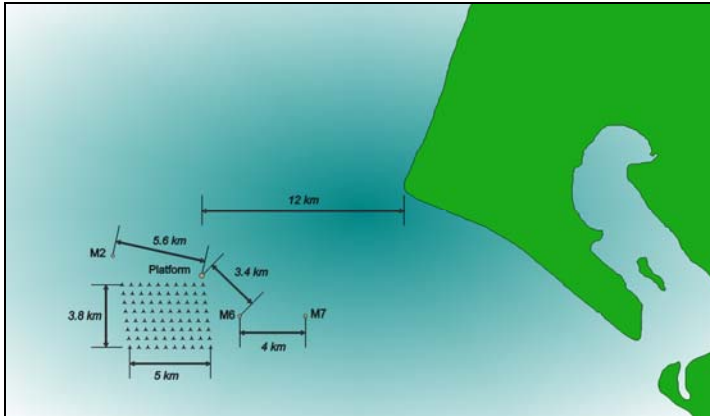


Figure 2.5. Description of the Horns Rev wind farm.

The wind turbines are Vestas V80 which have hub heights at 70 m AMSL. The rotor diameter is 80 m; thus the blade tip reaches 110 m AMSL at the upper blade position. A more detailed description of the turbine is given in Figure 2.6.

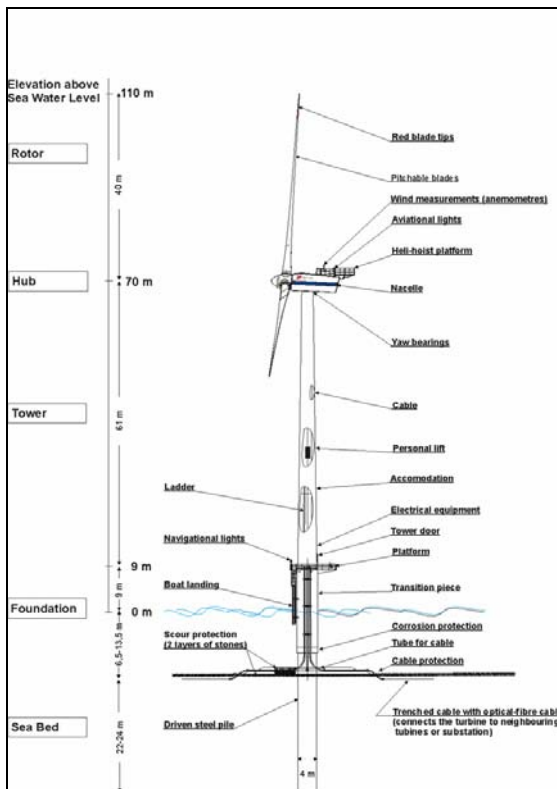


Figure 2.6. Description of the Vestas V80 wind turbine. Courtesy of DONG energy.

### 2.1.2 Meteorological masts

Three meteorological masts are installed in the neighborhood of the wind farm. Firstly, Mast 2 (M2) was erected in 1999 for the assessment of the wind resource and sea conditions during the wind farm planning. Secondly, Masts 6 (M6) and 7 (M7), the twin masts, were erected mainly to observe the wind farm wake when the wind comes from

the westerly sector. The transformer/platform of the wind farm is located at the North-east part. The geographical coordinates of the masts and the platform are given in Table 2.1.

*Table 2.1. Geographical coordinates of the masts and the platform at Horns Rev.*

Station	Latitude	Longitude	Distance to the closest turbine
M2	55°31'08.81''	7°47'15.07''	2 km North
M6	55°29'12.54''	7°54'43.56''	2 km East
M7	55°29'14.16''	7°58'31.20''	6 km East
Platform	55°30'31.03''	7°52'27.76''	0.5 km North

All three masts have lattice structures with square cross-sections and are instrumented with cup anemometers, wind vanes, temperature sensors at different levels (see Figure 2.7). M2 is also instrumented with relative humidity, pressure, irradiation and rain sensors. M6 and M7 have their own measurements of air pressure. The data logging system collects the observations at 2 Hz. 10 min (minutes) mean values are stored in the wind farm owners database. The instrumentation at each mast is given in Table 2.2. More detailed information concerning the meteorological system is given in Elsam Engineering, 2005.



*Figure 2.7. Photograph of M6. Courtesy of DONG energy.*

Table 2.2. Instrumentation of the masts at Horns Rev. (NE=North-East, SW=South-West, NW=North-West and SE=South-East).

Mast	Height AMSL [m]	Instrument	Position on boom
M2	62	1 Cup anemometer [ $\text{ms}^{-1}$ ]	Top
	45	2 Cup anemometers [ $\text{ms}^{-1}$ ]	SW & NE
	30	2 Cup anemometers [ $\text{ms}^{-1}$ ]	SW & NE
	15	2 Cup anemometers [ $\text{ms}^{-1}$ ]	SW & NE
	60	Wind vane [Deg.]	SW
	43	Wind vane [Deg.]	SW
	28	Wind vane [Deg.]	NE
	55	Temperature [ $^{\circ}\text{C}$ ]	NE
	13	Temperature [ $^{\circ}\text{C}$ ]	NE
	-4	Temperature [ $^{\circ}\text{C}$ ]	Sea
	13	Air relative humidity [%]	NE
	55	Air pressure [hPa]	NE
	13	Irradiation [ $\text{Wm}^{-2}$ ]	SW
	13	Rain detector [mm]	SW
M6 & M7	70	1 Cup anemometer [ $\text{ms}^{-1}$ ]	Top
	60	1 Cup anemometer [ $\text{ms}^{-1}$ ]	NW
	50	2 Cup anemometers [ $\text{ms}^{-1}$ ]	NW & SE
	40	1 Cup anemometer [ $\text{ms}^{-1}$ ]	NW
	30	2 Cup anemometers [ $\text{ms}^{-1}$ ]	NW & SE
	20	1 Cup anemometer [ $\text{ms}^{-1}$ ]	NW
	68	Wind vane [Deg.]	NW
	28	Wind vane [Deg.]	NW
	64	Temperature [ $^{\circ}\text{C}$ ]	SE
	16	Temperature [ $^{\circ}\text{C}$ ]	SE
	-4	Temperature [ $^{\circ}\text{C}$ ]	Sea
	16	Air pressure sensor [hPa]	SE

### 2.1.3 Wind conditions

A general overview of the wind conditions at Horns Rev is presented in Figure 2.8 which represents the annual observations.

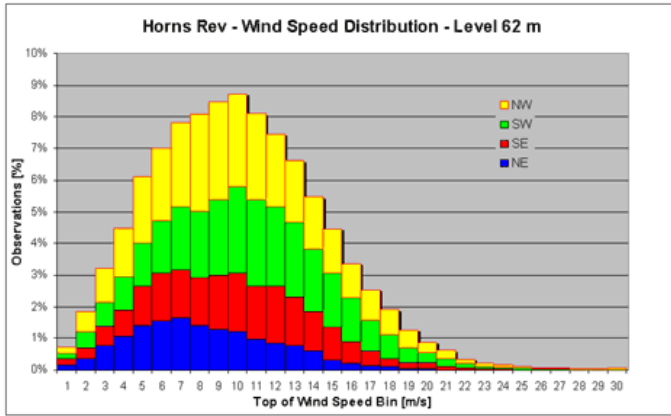


Figure 2.8. Wind speed distribution on M2 at 62 m AMSL. Courtesy of DONG energy.

The mean wind speed is around  $10 \text{ ms}^{-1}$  at 62 m AMSL on M2. It can be seen from the figure that more than 10% of the wind speed observations are above  $15 \text{ ms}^{-1}$  where the North-West and South-West sectors register higher wind speeds (the open sea sectors) than the easterly sectors where the land is located. The wind distribution on M2 is shown in Figure 2.9 at 62 m AMSL for different sectors.

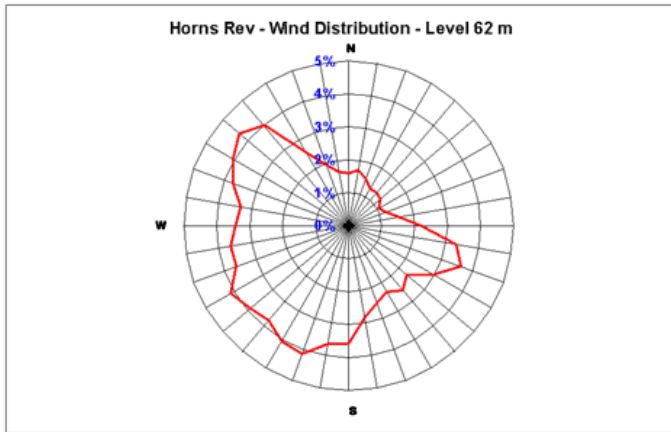


Figure 2.9. Wind distribution on M2 at 62 m AMSL for different sectors. Courtesy of DONG energy.

The wind is dominated at Horns Rev by the westerly sectors. In this way, the wake of the wind farm is often observed at the east masts (M6 and M7). For further analysis on wind direction from open sea, land and wind farm wake refer to (Peña *et al.* 2007).

## 2.2 Meteorological observations (up to 70 m)

Observations from the three different meteorological masts (provided by DONG energy) were available during the six-month campaign's period in which both LiDAR and SoDAR were installed at platform.

The distribution of the wind in different sectors (separated each 30°) is shown in Figure 2.10 from the wind vanes at the three different masts.

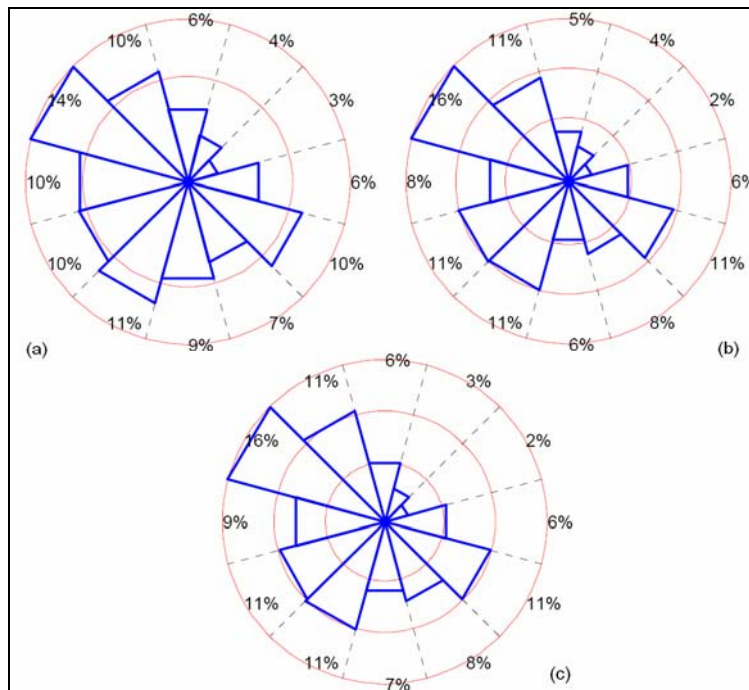


Figure 2.10. Wind distribution on each sector. (a) M2 at 60 m AMSL. (b) M6 at 68 m AMSL. (c) M7 at 68 m AMSL.

The dominant sectors during the period of the campaign are the westerly open sea wind sectors. In particular, most of the measurements lay on sector 11 (where sector 1 corresponds to the northern sector at 0°, clockwise), whereas sectors 2 and 3 are the less populated.

As it is given in Table 2.2, the majority of the different levels on the masts have two different cup anemometers separated 180°. In the case of M6 and M7, they are placed at the North-west and South-east sectors. For M2, they are on the South-west and North-east sectors. Due to cup-malfunctioning detected at the level 15 m AMSL on the North-east cup at M2 and at the level 30 m AMSL on the South-west cup at M7, the following analysis corresponds to measurements from the westerly cup anemometers. In this way, the wind speed profile will correspond to measurements performed on the same “row” of cup anemometers where the westerly wind directions are the most populated sectors.

## 2.2.1 Mast distortion

The measurement of wind speed and turbulence performed with the cup anemometers can be influenced by different sources of error, apart from the inherent calibration errors and cup over-speeding which are assumed to give small uncertainties (Pedersen, 2004). These are:

1. Direct flow distortion by mast shade: In Figure 2.11 is shown a cross-section of M6 and M7. The direct mast shade is avoided by rejecting all measurements on the influenced sector. The direction is detected by looking at the variation of wind speed ratio with the direction (from two cup anemometers at the same level). This is performed for M2 and M6 in Figure 2.12.

It is simple to distinguish the region affected directly by the mast shade in Figure 2.12 from the pronounced peaks of relative wind speed. It is interesting to note that the cup anemometers at M2 are not located at the directions 45 and 235° (as it is normally assumed) but they are shifted 30°.

2. Non-direct flow distortion: The booms, mast and other parts of the structure also influence the cup measurements beyond the direct mast shade. The effect of the mast on the cup anemometer observation of wind speed is studied at each level on M2 and M6. The analysis of the air flow around a lattice structure (like the masts at Horns Rev) is performed as in IEC, 2005. A series of iso-speed plots is shown in Figure 2.13 for seven different positions of the boom relative to the wind direction  $\theta_{rel}$ .

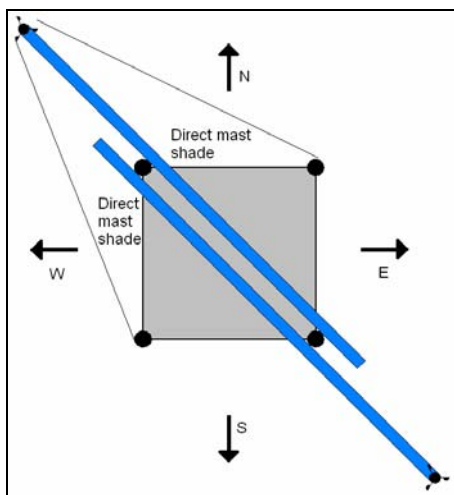


Figure 2.11. Cross-section of M6 and M7 indicating the direct mast shade.

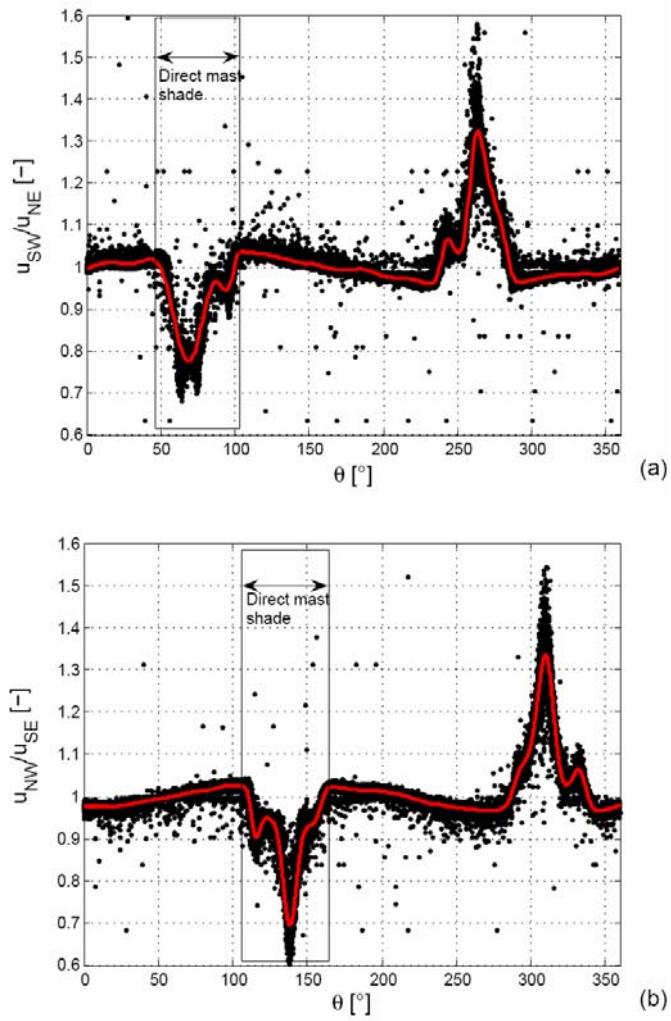


Figure 2.12. Relative cup anemometer wind speed variation with direction. (a) M2 at 45 m AMSL. (b) M6 at 30 m AMSL.

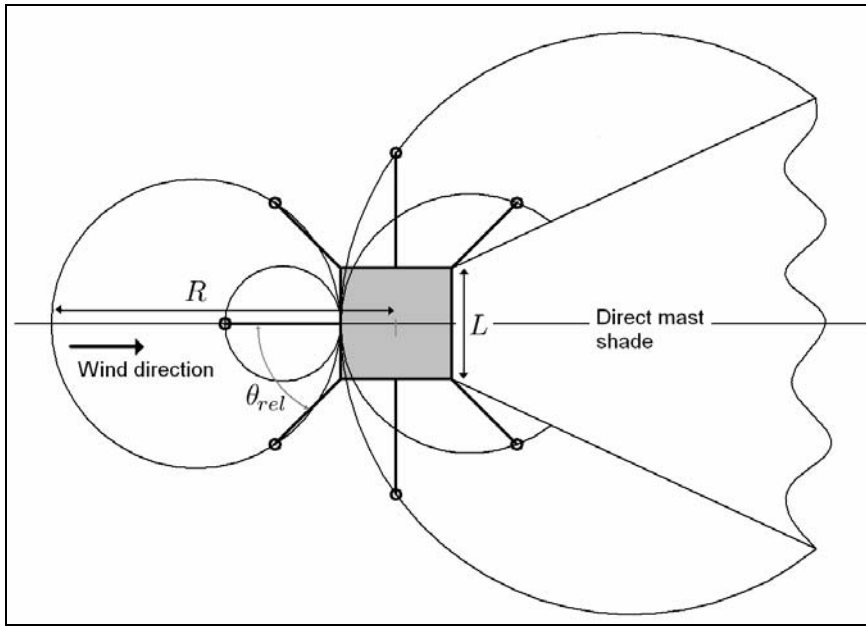


Figure 2.13. Plots of flow iso-speed around a square lattice mast.

The values of the iso-speed at the different “circles” can be determined by measuring the distance  $R$  of the extended circle formed at each boom position. The wind speed deficit  $u_d$  is computed on the center line (aligned with the wind direction) as:

$$u_d = 1 - \left( 0.062C_t^2 + 0.076C_t \right) \left( \frac{L}{R} - 0.082 \right) \quad (2.1)$$

where  $L$  is the length of the mast cross-section and  $C_t$  is the thrust coefficient. This coefficient can be estimated for a square latticed mast by:

$$C_t = 2.6(1-t)t \quad (2.2)$$

where  $t$  is the mast solidity. The solidity of the structure at the different sections on the masts is computed using the geometry of the structure. The variation of wind speed deficit with direction (relative to the wind) applying Eq. (2.1) is shown in Figure 2.14 for the different masts at the different observation levels.

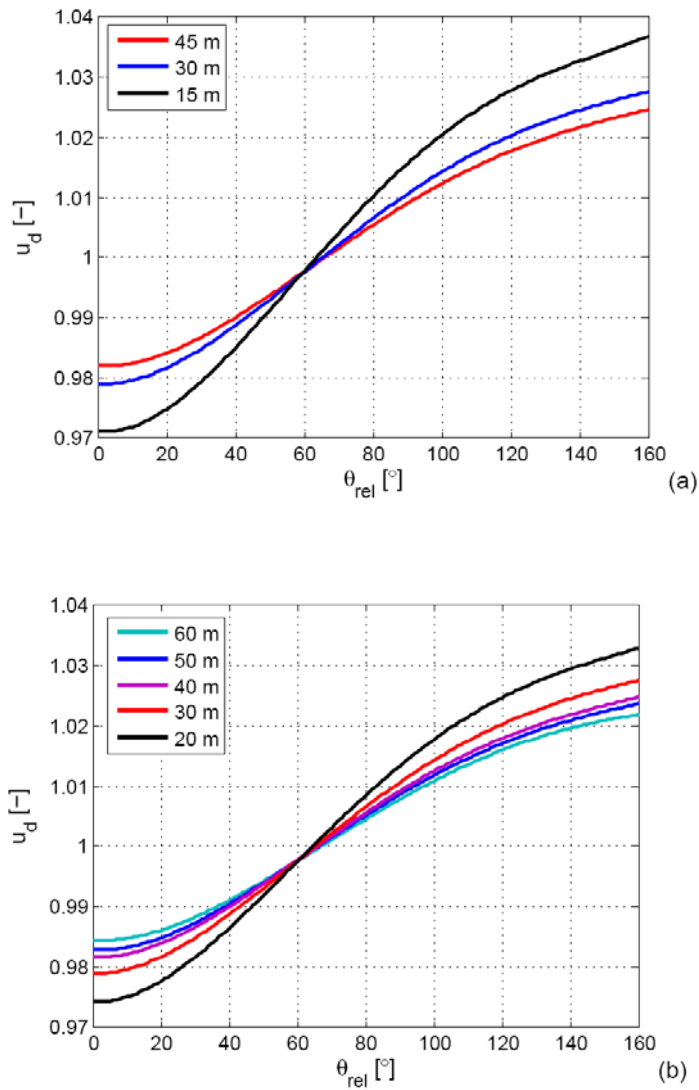


Figure 2.14. Variation of the wind speed deficit/increment at each level with relative wind direction. (a) M2. (b) M6 and M7.

There are two different distortion regions according to the results of the IEC model in Figure 2.14. The observations at the cups are lower than the “absolute” wind speed for the first 60 to 65° of relative angle between the boom and the wind direction. At greater angles, the cup anemometers observe a higher wind speed before the region of direct mast shade is reached. The deficits/increments are greater at lower levels mainly due to the increase of solidity near the mast base. The level of uncertainty of the wind speed from the cup anemometer measurements is around 2 to 3% for the extreme values.

### 2.2.2 Observed mean wind speed

The observations of 10 min mean wind speeds from the cup anemometers are compared for the three masts in Figure 2.15. The mean wind speed is restricted to values above  $2 \text{ ms}^{-1}$ . The comparison is made for all wind directions.

A linear regression was applied to the data and is shown on each comparison. Both applied linear regressions show very high correlations, especially for M6 and M7 which are the closest masts. The wind farm wake which is observed by M2 on a different angle than M6 and M7 may cause the lower correlation in Figure 2.15(a).

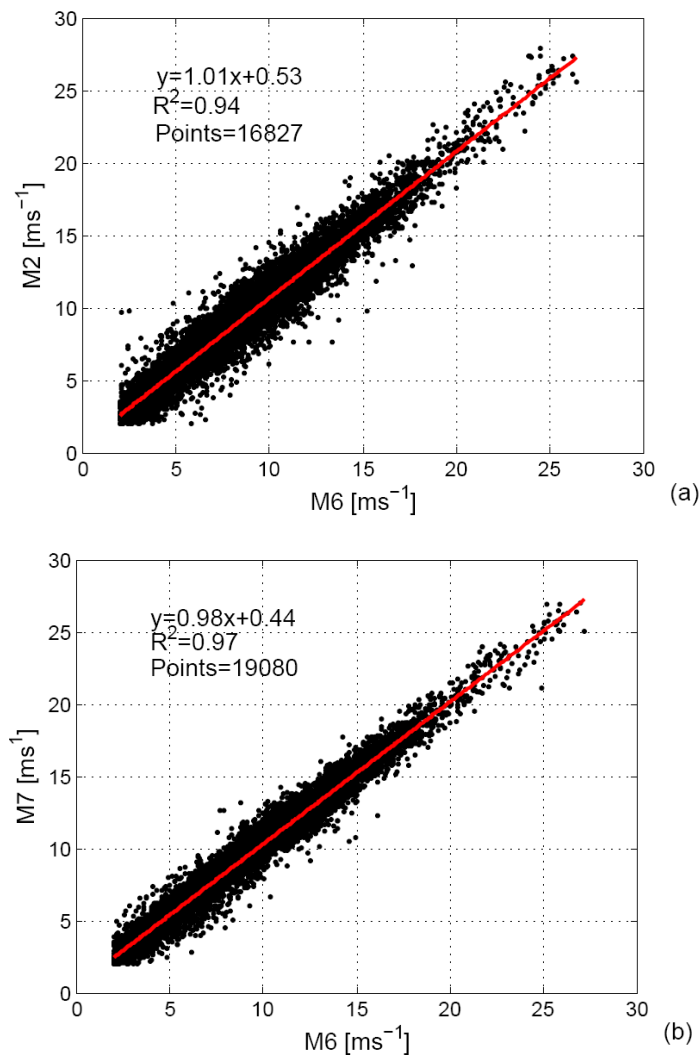


Figure 2.15. Comparison of observed mean wind speeds at the cup anemometers. (a) M2 at 62 m and M6 at 60 m AMSL. (b) M6 and M7 at 70 m AMSL.

The high degree of correlation of the mean wind speed measurements at Horns Rev is due to the high homogeneity of the flow. This will allow us to compare the measurements from the cups to the observations performed at the platform where the LiDAR and the SoDAR were installed.

### **2.2.3 Mean wind speed profiles**

Profiles of mean wind speed can be derived from the cup measurements performed on the masts. This is shown in Figure 2.15 for the three masts on the 12 different wind sectors. For each sector, the number of individual 10 min profiles is also given where the same amount of measurements are performed at the different levels.

It can be seen in the Figure that the sectors 8, 9 and 12, which are facing the open sea, show the highest mean wind speeds, whereas sectors 1 and 2 the lowest (sectors 3, 4 and 5 have the lowest amount of measurements and therefore are taking out in the graphs at certain mast positions).

The figure shows that the measurements taken from all the top-mounted cup anemometers - at the different masts - do not follow the behavior of the logarithmic wind speed profile well. The wind speeds appear to be higher. As it is shown in Figure 2.14, the measurements at the lower cup anemometers can be flow distorted. For the easterly sectors, the cup anemometers observe a higher wind speed according to the model; thus if these measurements are corrected the wind speed will be lower and the difference between the lower cup anemometers and the top-mounted observations will be greater. This is an indication of a speed up effect due to the structure at the top-mounted cup anemometers which have been previously studied in Perrin, 2007.

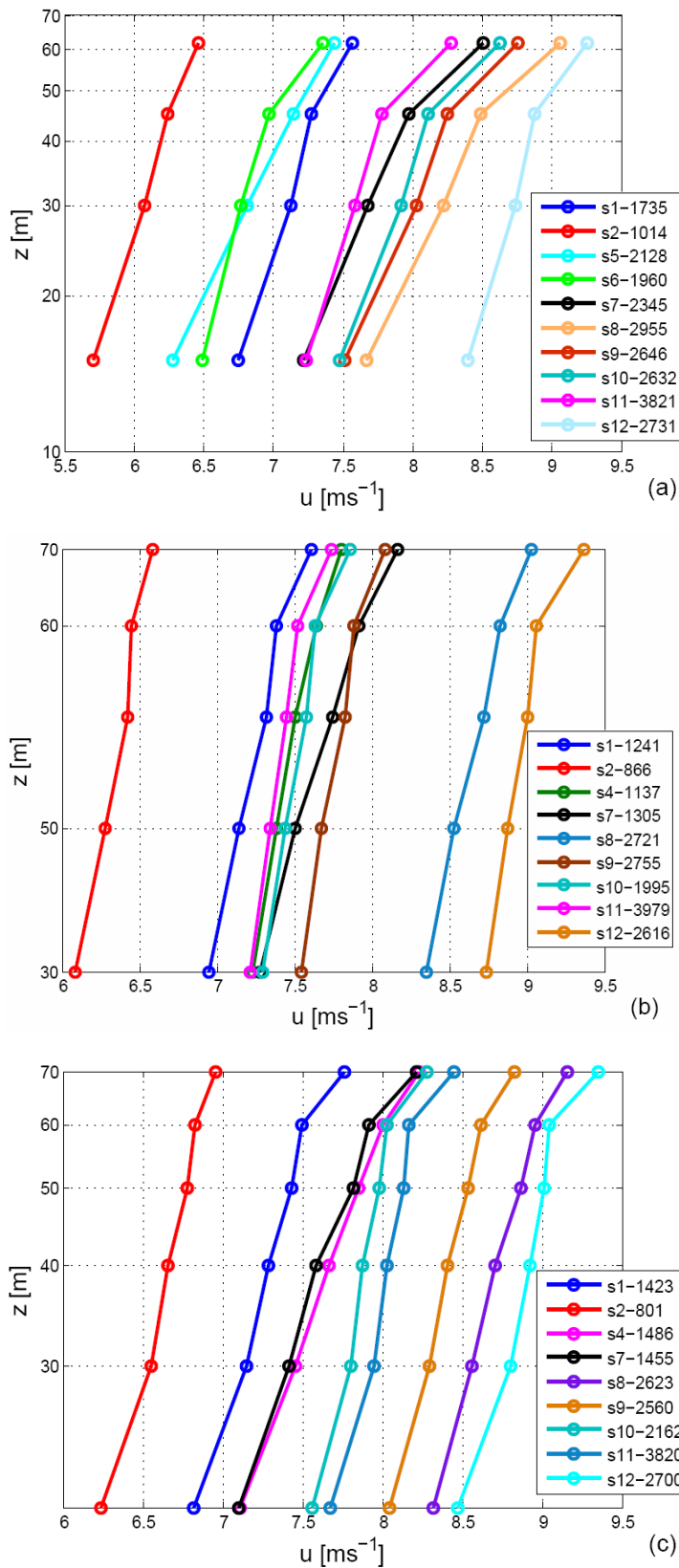


Figure 2.16. Mean wind speed profiles for different sectors at the masts. The number of individual 10-min profiles is given in the legend. (a) M2. (b) M6. (c) M7.

## 3 The ZephIR LiDAR profiler (up to 160 m)

Michael Courtney

We have used a ground-based, remote sensing instrument commonly known as a LiDAR (more properly a doppler profiling LiDAR) to measure the wind speeds above the offshore platform. The basic LiDAR principle relies on measuring the Doppler shift of the radiation from a coherent laser, scattered by natural aerosols, which are carried by the wind. The Doppler-shifted frequency is directly proportional to wind speed along the line of sight, so the LIDAR instrument in principle needs no calibration.

### 3.1 The ZephIR LiDAR – theory of operation

Previous offshore profile measurements (Antoniou *et al.* 2006) used a prototype LiDAR from the English company Qinetiq that had been developed in collaboration with Risø. Direct comparisons made with conventional mast-mounted anemometer measurements on land at Høvsøre have shown extremely good correlation in wind speed and direction (Antoniou *et al.*, 2004a). A thorough technical and theoretical description of this instrument is given in (Smith *et al.* 2007).

For the campaign at Horns Rev we used one of the units (number 8) from the first batch of commercially available LiDARs from Qinetiq, known as the ZephIR. Technically, the ZephIR is very similar to its prototype predecessor but has a design and packaging that is much more appropriate for field use.

The ZephIR is a continuous wave LiDAR operating at the eye-safe wavelength of 1.5 microns, with height discrimination achieved by focusing sequentially at a number of pre-programmed heights. By passing the focused laser beam through a continuously rotating prism, the beam forms a cone at 30° to the zenith (figure 3.1). In any given azimuth direction, the LiDAR measures the radial (or line of sight) velocity that contains resolved components of the horizontal and vertical wind speeds according to the equation

$$V_{rad} = |U \cos(\theta - \theta_d) \sin(\phi) + W \cos(\phi)| \quad (3.1)$$

where  $\theta$  is the instantaneous azimuth angle,  $\theta_d$  the wind direction.  $\phi$  the angle of the cone and  $U$  and  $W$  the horizontal and vertical speeds respectively. Under the assumption that the flow is uniform throughout the entire measuring volume, the three unknowns in this equation,  $U$ ,  $W$  and  $\theta_d$  can be obtained using a non-linear least squares method applied to the measured dataset  $(\theta, V_{rad})$ .

Backscattered, Doppler shifted light from the focus volume is mixed with the baseband light and the power of the resulting beating is measured in the LiDAR's photo detector. The analogue signal is sampled at 50MHz and converted at 200kHz to power spectra using a 256 point (time domain) FFT. In order to obtain an acceptable signal to noise ratio, even in reasonably clean air, 4000 of these spectra are ensemble averaged to provide one Doppler spectra every 20 ms, corresponding to 7.2 degrees of azimuth. From each of these spectra the frequency of the peak value is obtained by calculating the centroid. This frequency corresponds linearly to the radial velocity for this azimuth.

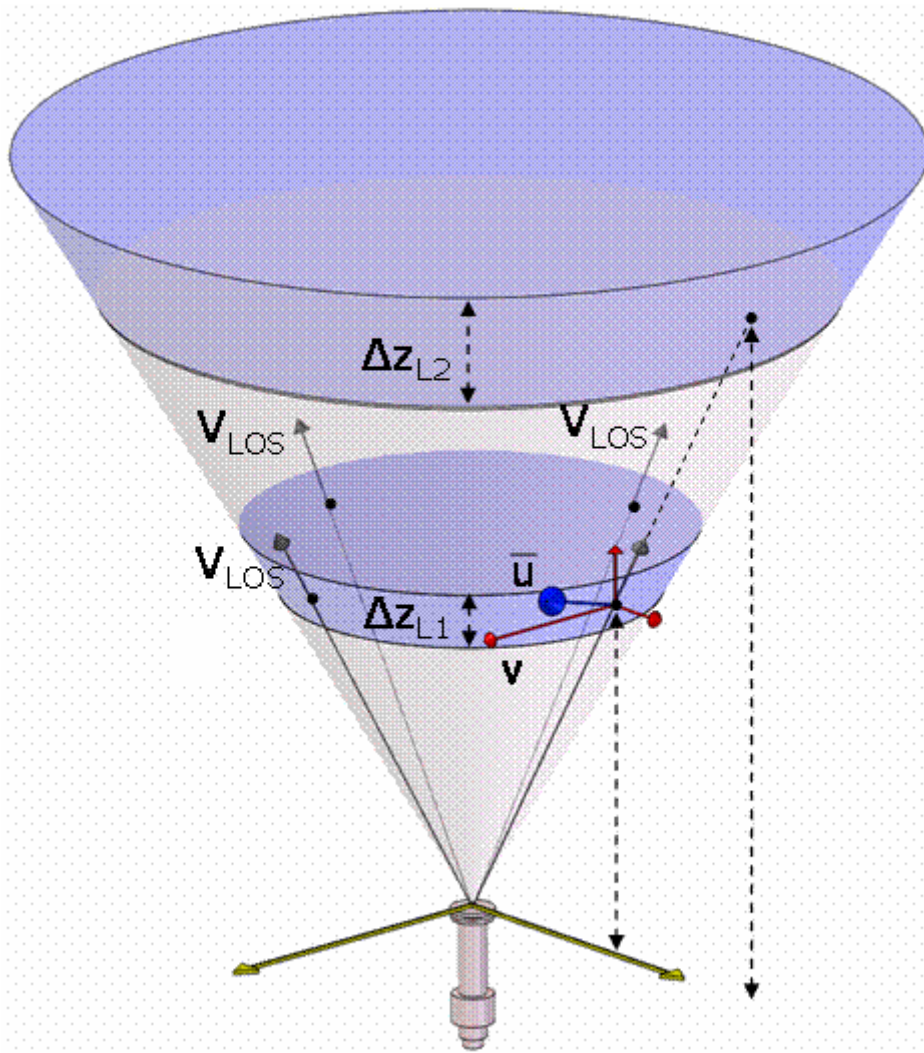


Figure 3.1 Sketch of the observational volume of a focused LIDAR.

In the current configuration, the ZephIR measures over 3 complete rotations of the prism at each of the programmed heights, taking exactly 3 seconds and providing 150 radial velocity measurements. When represented in a polar plot ( $V_{rad}$  vs. azimuth), the measurements ideally form a figure of eight (figure 3.2). The three unknowns,  $U$ ,  $W$  and  $\theta_d$  are obtained by using a Levenburg-Marquadt (LM) procedure. As starting conditions,  $U$  is set to the maximum radial velocity,  $W$  is set to zero and  $\theta_d$  to the azimuth for the maximum velocity.

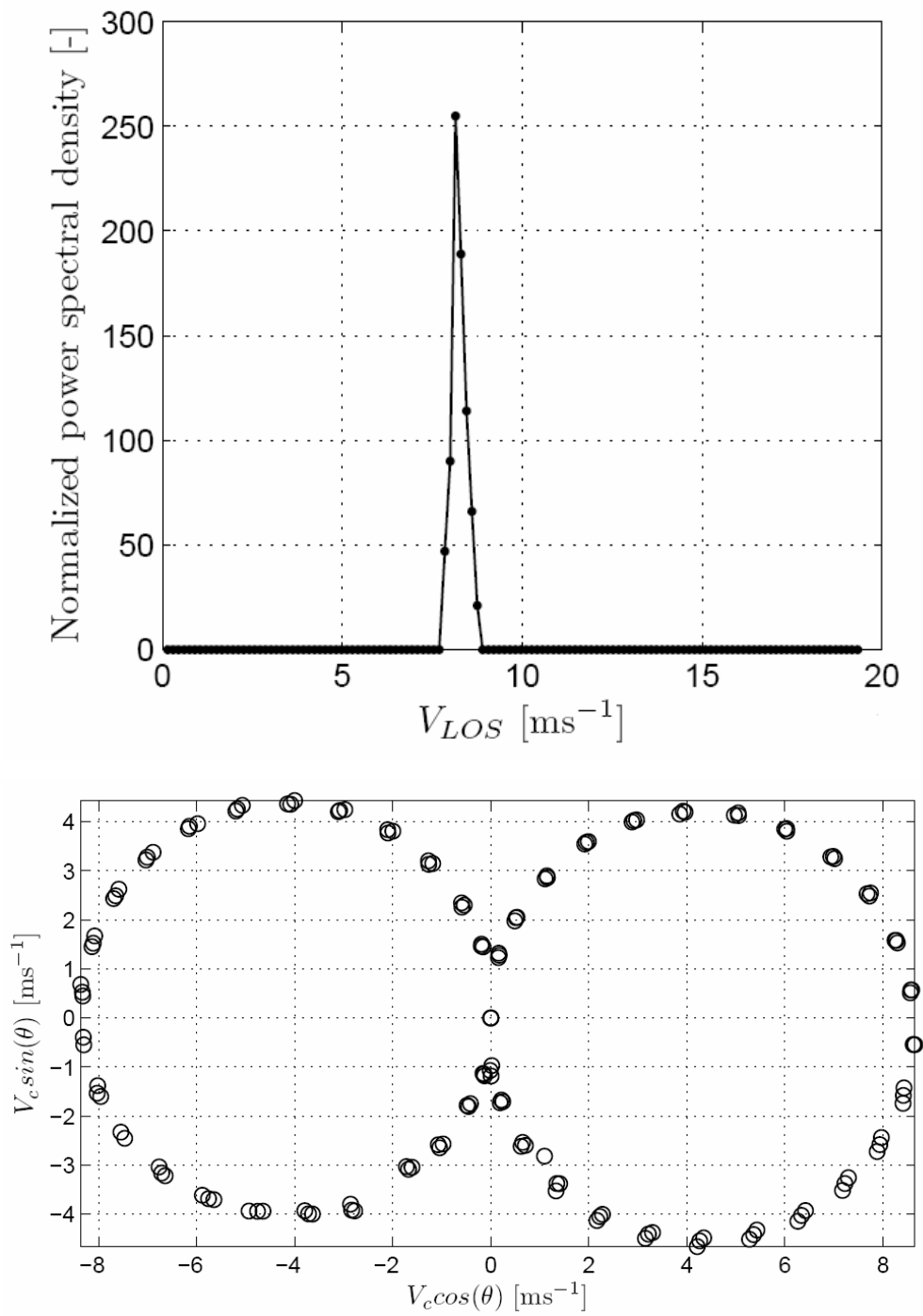


Figure 3.2 (top) Averaged Doppler-shifter spectrum at one single scan at 121 m height (bottom) Figure of eight showing the measurements at 121 m during the 3 second period.  $V_c$  corresponds to the centroid velocity value of each averaged Doppler-shifted value. (also submitted to Wind Energy by Peña et al.).

As implied in equation 3.1, the sign of the Doppler shift (and hence the sign of the radial velocity) is lost in the signal processing. This happens because the backscattered light is mixed with the baseband (the laser source) frequency itself. In this case a frequency shift of  $+Af$  and  $-Af$  give precisely the same beating pattern and can not be distinguished from each other. Because of the rectification of the radial velocity, there are actually two possible solutions to equation 3.1. The signs of the direction and the vertical speed (although not their internal relationship) are ambiguous. We know the axis of the wind direction, but not from which side it blows. For this reason the ZephIR is equipped with a thermal wind sensor mounted at the top of a small met mast. Of the two wind directions possible from the fitted data, the one closest to the value from the wind sensor is chosen. If it is necessary to change the sign of the wind direction, then the sign of the vertical velocity must also be swapped in order to maintain the correct internal relationship.

Two levels of data are stored by the ZephIR on a removable 4GB compact flash disk. The speeds and direction obtained from each of the 3 second datasets, representing one height, are stored together with a so-called ‘turbulence parameter’. This latter is in fact, a measure of the ‘goodness of fit’ and as such is influenced mainly by turbulent fluctuations (within the 3 second measuring period) but also by noise and other error conditions such as cloud effects (see below).

The 50 Hz Doppler spectra are also saved on the flash disk, consuming a vast majority of the available storage. Unfortunately, the ZephIR internal software is unable to compress this data. In practice, since the spectra have been thresh-holded to remove noise, most of the spectral estimates are zero and there is a huge redundancy. The files can actually be compressed to about 10% of their original size. In their uncompressed form, there is only room for 4 days spectra on the compact flash card.

Ten minute mean values and standard deviations can also be extracted from the ZephIR but are calculated ‘on the fly’ from the stored 3 second data. It should be noted that one measurement at one height takes 3 seconds. The focus is then moved to the next height and a new 3 second period begins. Including the time for re-focusing, a complete cycle of 5 heights takes about 18 seconds. In one ten minute period at each height there will be around 33 samples, each scanned over a period of 3 seconds and with about a 15 second gap between each. Whilst the mean value is essentially unaffected by this sampling pattern, the standard deviation is calculated from the 3 second samples. This averaging time and its corresponding spatial volume are crucial in interpreting the values obtained. This is explained in detail in section 3.2.

### 3.2 Measurement imperfections

Inherent in the design of a focused LiDAR system is that the vertical measuring length (the probe length) increases with the square of the measuring height. For the optics of the ZephIR, the probe length is about 20m at 100m measuring height. Above 150m, the probe length becomes unacceptably large and this represents the upper limit of measuring height for this design.

Within the measuring volume the intensity of the focused beam and, assuming a constant aerosol profile, the backscatter intensity, is weighted vertically by a Lorentzian function with a maximum at the focus point. Linear profiles will weight symmetrically about the focus point and in theory the LiDAR will report exactly the same mean speed as from a point measurement at the focus point, despite the finite probe length. This is not the case

for non-linear profiles and this can introduce a small error. For a logarithmic profile, the error is typically about 0.15% at 100m.

The assumption of a constant aerosol profile is not always entirely justified but for the small probe lengths at lower measuring heights, it is not unreasonable. A vertical variation of aerosol concentration within the measuring volume will affect the weights of the backscatter from the various heights (it has to be combined with the Lorentzian function). Normally we expect only a small variation over the probe length and this is not expected to be a significant source of error.

An extreme case of aerosol non-uniformity that we are obliged to consider is when low clouds are present. The backscatter coefficient from the water droplets at the base of the cloud is several orders of magnitude higher than from the background aerosol. Even though the cloud base (say at 1500m) is way outside the focal range, the cloud backscatter, Doppler shifted at the speed of the cloud, is so intense that it can be of comparable or larger magnitude than the focused backscatter from the nominal measuring height when measured at the photo-detector. Unless corrected for, this spurious spectral content will normally result in an over-estimation of the wind speed (since clouds are higher and therefore usually faster).

The ZephIR has a cloud-correction algorithm based on an attempt to measure and correct for the spectral content from the clouds, by focusing at an extra, higher height, usually 300m. This spectral content is then simply subtracted from the spectra measured for the lower heights (actually on a per azimuth basis). Unfortunately the ZephIR makes no attempt to distinguish between cloud backscatter and background aerosol backscatter in the 300m measurement. Whilst the algorithm is moderately successful at removing cloud contamination, it continues to perform the 'correction' even when clouds are absent. This results in a general degradation of the LiDAR measurements.

The internal cloud-correction algorithm has not been used for the Horns Rev measurements. Instead we have attempted to identify periods with low clouds from the ratio of the backscatter at the different heights. The idea here is that with no cloud present, the backscatter from all heights will be approximately equal (a general characteristic of a focused system). When low clouds are present, they will appear with larger amplitude as the focus moves to higher heights since they will be increasingly more in focus (or less out of focus). Higher focus heights will therefore have a significantly higher backscatter than lower heights. Such periods are filtered from the final data set.

### **3.3 Experimental setup and system operation**

The LiDAR was installed on the platform at a position that is 20m AMSL. Initially AMSL measuring heights of 46, 63, 91 and 121m were chosen. From visual inspection of the LiDAR data, significant non-zero vertical velocities could be seen for the lowest height, indicative of flow distortion due to the platform structure. It was therefore decided to abandon the lowest measuring height and instead increase the upper limit of the profile by 40m. We thus ended with the measuring heights of 63, 91, 121 and 161m AMSL. A fifth LiDAR measuring height of 300m (320m AMSL) was used to provide spectral data pertaining to cloud presence.

The ZephIR measures autonomously (given an available 220Vac power supply) and stores processed data on a 4GB compact flash card. Data can be accessed either remotely using a GSM link, locally over a network connection or by physically removing the flash

card (from under two panels) and copying the data directly to a computer. Remote access with GSM is so slow that it can only be used for checking system operation and retrieving 10 minute mean values of the measured data. Physical access to the LiDAR was impractical and very costly at the offshore platform. In order to save data at the lowest level of processing (the 50 Hz Doppler spectra) and at the same time, avoid frequent trips to the platform, a pc was dedicated to receive spectra streamed from the LiDAR. This pc was placed on the wind farm's network, giving access to the internet for outgoing data and permitting remote-control via a VPN link.

Initially this pc was placed at the land end of the wind farm network in Esbjerg. The LiDAR and pc communicated directly over the network. It became quickly apparent that the communication protocol between the LiDAR and pc requires a very low level of extraneous traffic on the network. This could not be accomplished with the two systems physically separated and as a consequence the pc was moved out to the platform and provided with a private network connection to the LiDAR.

Spectra were streamed to the pc using a modified version of the pc host program supplied with the ZephIR. The data were saved as hourly files. These were compressed (to around 10% of their original size), stored on the local hard disk and also transmitted to Risø using a standard ftp protocol.

After re-locating the dedicated pc out to the offshore platform, close to the LiDAR, the system reliability improved considerably. However, the Qinetiq software was a relatively early version and not completely stable. The streaming would stop irregularly with a mean interval of about 3-5 days. Using the remote-control connection from Risø, we were always able to re-start the software but this problem caused a significant fall in the data availability.

A more serious problem occurred on 8 June 2006. Contact to the LiDAR was lost and could not be re-established. No further data were recorded until 24 August 2006, following a trip to the offshore platform. The failure was caused by salt water leaking into the (external) LiDAR power supply. Fortunately, the necessary spare parts were available and this could be repaired on-site. An improvement to the waterproofing of the power supply box was improvised (insulating tape and a plastic bag) and the problem did not recur.

Overall, the LiDAR was available for 52% of the measuring period. Excluding the power supply failure period, the LiDAR availability was 88%.

### **3.4 Data management and processing**

All the raw data received from the offshore LiDAR have been entered into a database. This database forms the core of our data management system and processing of the data takes place within this context. Conversion of the raw Doppler spectra to fitted 3 second speeds and direction takes place using an algorithm that is very close to that used internally by the LiDAR. In cases where both spectra and LiDAR processed 3 second data have been available, there has been close agreement between the Risø and ZephIR calculated data sets. Some intermediate discrepancies have been identified but these have been traced to errors in the Qinetiq algorithm that have subsequently been repaired. The data presented in this report are calculated using the Risø algorithm.

Results from the fitting algorithm are stored in a new table and subsequently used to calculate 10 minute statistics (mean and standard deviations) of the horizontal and vertical speeds. Since the streamed spectra contain no information from the ZephIR met sensor, we have no information about the local wind direction. However, detailed wind direction measurements are available from the wind farm masts and therefore no attempt has been made to further analyze the LiDAR direction data.

Ten minute statistics of the LiDAR wind speeds are the primary level of data in this report and of course are stored in their own database table. The wind farm mast data is available only at the ten minute level. Each mast has been assigned its own database table. Consistent time-stamping is used throughout the database (with all start contra stop time issues resolved) allowing rapid, flexible and consistent querying with joins between all the pertinent data sources.*Mike Courtney*

We have used a ground-based, remote sensing instrument commonly known as a LiDAR (more properly a doppler profiling LiDAR) to measure the wind speeds above the offshore platform. The basic LiDAR principle relies on measuring the Doppler shift of the radiation from a coherent laser, scattered by natural aerosols, which are carried by the wind. The Doppler-shifted frequency is directly proportional to wind speed along the line of sight, so the LIDAR instrument in principle needs no calibration.

## 4 Theory on LIDAR and turbulence

Torben Mikkelsen

### 4.1 The ZephIR LIDAR's Spatial Measurement Volume

The purpose of this note is to investigate the spatial filter function of the QinetiQ Ltd. Coaxial ZephIR wind LiDAR system.

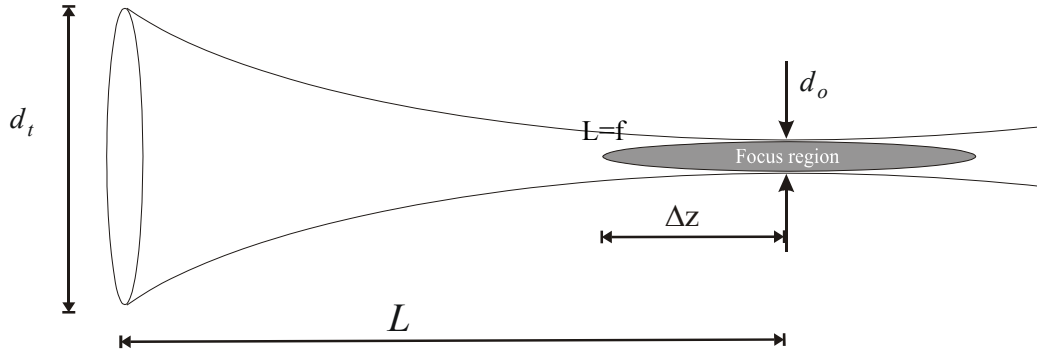


Fig.4.1 Definitions for the LiDAR's focused laser beam (The numbers in parenthesis applies to the QinetiQ ZephIR LiDAR at focal length).

The LiDAR's effective measurement volume is in the along-beam direction limited to the confocal region. This result in an along-beam space-weighted function, which to a good approximation is proportional to the beam intensity  $I$

Assuming a Gaussian beam approximation, the beam intensity near the focal point is a rotational-symmetric "cigar-shaped" volume, with a 2-D Gaussian crosswind beam intensity distribution (with  $\sigma_y = \sigma_z = d(\Delta z)$ ) and an along-beam intensity given by a Cauchy function, viz.:

$$I(\Delta z) = \frac{P_t}{A(\Delta z)} = \frac{P_t}{\pi (d(\Delta z)/2)^2} = \frac{I_0}{1 + (\Delta z/z_R)^2} \quad (4.1)$$

$$= \frac{1}{\pi} \frac{z_R}{z_R^2 + (\Delta z)^2} \cdot \pi z_R I_0 = \pi z_R I_0 \cdot C(\Delta z) \text{ [Watt/m}^2\text{]}$$

where  $Z_R$ , the Rayleigh length, denotes the "Half Width at Half Maximum" (HWHM) parameter of the Cauchy distribution, also called the Lorentzian distribution or Lorentz distribution function.

The focal-volumes radial weighting function can consequently be approximated by a Cauchy (Lorentz) distribution of the form

$$C(r') = \frac{1}{\pi} \frac{z_R}{z_R^2 + (r')^2} \quad (4.2)$$

with  $\Delta z = r' = L - \langle L \rangle$ , where  $\langle L \rangle$  is the focal point  $f$ , and where the distributions width parameter (half width at half maximum) is identical to the Rayleigh length parameter,  $z_R$ .

Table 4.1: The ZephIR LiDAR's Optical Parameters.

---

Parameters in this table is calculated for a focal length  $L = f = (100 \text{ m})$

ZephIR's aperture<sup>1</sup> diameter:  $d_t = (0.048 \text{ m})$

---

i) The focused beam minimum waist diameter

$$d_o = \frac{4\lambda f}{\pi d_t} = \left( \frac{4 \cdot 1.55 \cdot 10^{-6} \cdot 100}{3.14 \cdot 0.048} \approx 4.11 \text{ mm @ } L=100 \text{ m} \right)$$

ii) The Rayleigh length

$$z_R \equiv \frac{\pi \left(\frac{d_o}{2}\right)^2}{\lambda} = \frac{\pi d_o^2}{4\lambda} = \frac{4\lambda f^2}{\pi d_t^2} = \left( \frac{3.14 \cdot 0.00411^2}{4 \cdot 1.55 \cdot 10^{-6}} \approx 8.5 \text{ m @ } L=100 \text{ m} \right)$$

iii) The far-field distance

$$D_{FF} \square \pi \frac{\left(\frac{d_t}{2}\right)^2}{\lambda} = \left( \pi \frac{0.024^2}{1.55 \cdot 10^{-6}} \square 1.2 \text{ km} \right)$$

iv) The ratio

$$\frac{D_{FF}}{z_R} = \pi \frac{d_t^2}{4\lambda} \Big/ \frac{\pi d_o^2}{4\lambda} = \frac{d_t^2}{d_o^2} \left( = \frac{0.048^2}{0.00411^2} \square 136 \text{ @ } L = 100 \text{ m} \right)$$

v) The "confocal" parameter"

$$2z_R$$

This quantity denotes the "width" within the measurement volume where the beam is approximately collimated (i.e. the plane wave approximation can be applied).

---

It can be shown<sup>2</sup> that the beam width  $d$  near the focal point is a symmetric function of  $\Delta z$

$$d^2(\Delta z) = d_0^2 \left( 1 + \left( \frac{\Delta z}{z_R} \right)^2 \right)$$

1 Radius is taken as the value where the intensity has dropped to  $e^{-2}$  of its value at the beam center; Ref. M. Harris (2006); NREL/TP-500-39154 p20.

2 Laserteknik; Torben Skettrup; Polyteknisk Forlag; Eqs. (16)

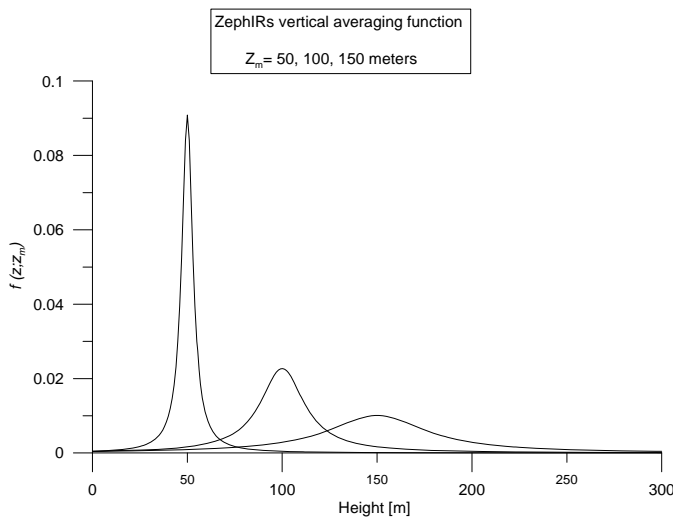
And that, correspondingly, that the ZephIR wind LiDAR's radial focal-volume weighting function can be approximated by a Cauchy (or Lorentz) distribution

$$C(r') = \frac{1}{\pi} \frac{z_R}{z_R^2 + (r')^2} \quad (4.3)$$

Here,  $\Delta z = r' = L - \langle L \rangle$ , where  $\langle L \rangle$  is the focal point  $f$ , and where the distributions width parameter (half width at half maximum) is coincident with the Rayleigh length parameter  $z_R$ .

The Rayleigh length  $z_R$  increases with the LiDAR's measurement range  $L$  to the second power, cf. Table I; ii), and, for the QQ ZephIR LiDAR, it can to a good approximation be parameterized as<sup>3</sup>:

$$z_R(L) \approx 0.00085 L^2 [m]$$



$$z_R(L) \approx 0.00085 L^2 [m] \quad (4.4)$$

Fig. 4.2 The ZephIR's spatial weighting function as function of height.

<sup>3</sup> In the UPWIND (2006) progress report QinetiQ states that the HWHM at range  $L=100$  meters has been determined experimentally to be  $\sim 8.5$  m. This is in agreement with the calculations in the QQ LiDAR Table 1 in this report (TM).

Setting the ZephIR's measurement height to 100 meters, the optical systems focal length  $L$  (with the fixed 30 degrees wedge) is 115,47 meters, and the corresponding "HWHM" parameter  $z_R$  can then be estimated to be  $8.5 \cdot (115.47/100)^2 \sim 11.3$  m. The Full Width at Half Maximum:

$FWHM = 2z_R$  for ZephIR measurements at  $z=100$  meters height, is therefore 22.6 m. Projections of the ZephIRs radial beam-measurement volume onto the horizontal plane correspondingly yield:  $22.6 \sin(30) \sim 11.3$  m, as a measure for the ZephIR's effective horizontal probe volume.

Correspondingly, its vertical effective probe volume is  $22.6 \cos(30) \sim 19.6$  m.

## 4.2 Turbulence seen by the QinetiQ ZephIR LiDAR:

### 4.2.1 The Effects of Conical scanning and Lorentzian Probe

The purpose of this section is to predict the effective turbulence obtained from horizontal “figure of eight” averaged scans obtained with the conically scanning coaxial ZephIR™ wind LiDAR system.

The starting point is the usual near-neutral Kaimal component spectra for the three velocity components on the horizontal, lateral, and vertical direction, respectively:

$$\begin{aligned}
 n S_u(n)/u_*^2 &= \frac{102n}{(1 + 33n)^{5/3}} \\
 n S_v(n)/u_*^2 &= \frac{17n}{(1 + 9.5n)^{5/3}} \\
 n S_w(n)/u_*^2 &= \frac{2.1n}{(1 + 5.3n^{5/3})}
 \end{aligned} \tag{4.5}$$

Here, the dimensionless frequency  $n$  has been defined as  $n = fz/U$ , where  $f$  is frequency in Hz,  $z$  is measurement height above the ground, and  $U$  is the (10-min averaged) mean wind speed.

By letting the upper non-dimensional frequency  $n_{max} = f_{max}z/U$  tend to infinity the corresponding definite integrals can be evaluated (u, v analytically, and w via Mathematica, cf. the figures in Eqs.(4.6). For comparison is added: the figures in parentheses ( ) are text book “standard” relations. The figures in (( )) come from Panofsky H.A. & J.A Dutton. Atmospheric Turbulence: Models and Methods for Engineering Applications; Wiley: New York (1984).

$$\begin{aligned}
 \frac{\sigma_u^2}{u_*^2} &= \int_0^\infty \frac{102}{(1 + 33n)^{5/3}} dn \square 2.15^2; & (2.5^2); & ((2.39^2)) \\
 \frac{\sigma_v^2}{u_*^2} &= \int_0^\infty \frac{17}{(1 + 9.5n)^{5/3}} dn \square 1.64^2; & (2.0^2); & ((1.98^2)) \\
 \frac{\sigma_w^2}{u_*^2} &= \int_0^\infty \frac{2.1}{(1 + 5.3n^{5/3})} dn \square 1.24^2; & (1.3^2); & ((1.25^2))
 \end{aligned} \tag{4.6}$$

To investigate the combined effect of spatial filtering, partly originating from the beam probe volume (the Lorentzian optical probe filter), and partly from the horizontal conical scanning, the Kaimal spectra are cast into dimensional form:

$$\begin{aligned}\frac{\sigma_u^2}{u_*^2} &= \frac{z}{U} \int_0^{n_{\max} U/z} \frac{102}{(1 + 33fz/U)^{5/3}} df \\ \frac{\sigma_v^2}{u_*^2} &= \frac{z}{U} \int_0^{n_{\max} U/z} \frac{17}{(1 + 9.5fz/U)^{5/3}} df \\ \frac{\sigma_w^2}{u_*^2} &= \frac{z}{U} \int_0^{n_{\max} U/z} \frac{2.1}{1 + 5.3(fz/U)^{5/3}} df\end{aligned}\quad (4.7)$$

Eqs.(4.7) can be re-written in the form

$$\begin{aligned}\sigma_i^2 &= \int_0^{n_{\max} U/z} S_i(f) df; \\ \text{where} \\ S_u(f) &= u_*^2 \frac{z}{U} \frac{102}{(1 + 33fz/U)^{5/3}} \left[ \frac{m^2}{s^1} \right] \\ S_v(f) &= u_*^2 \frac{z}{U} \frac{17}{(1 + 9.5fz/U)^{5/3}} \left[ \frac{m^2}{s^1} \right] \\ S_w(f) &= u_*^2 \frac{z}{U} \frac{2.1}{1 + 5.3(fz/U)^{5/3}} \left[ \frac{m^2}{s^1} \right]\end{aligned}\quad (4.8)$$

We next transform the above frequency spectra into wave number spectra to evaluate the effect of spatial filtering, by use of the following relations

$$\begin{aligned}S_i(f)df &= F_i(k_1)dk_1 \\ \frac{d\omega}{dk} &= U = 2\pi \frac{df}{dk} \text{ (I.e., Taylors frozen turbulence hypothesis)} \\ \omega &= 2\pi f = Uk_1 \\ f &= \frac{U}{2\pi} k_1; \quad f_{\max} = \frac{U}{2\pi} k_{1,\max} \Leftrightarrow k_{1,\max} = \frac{2\pi}{U} f_{\max} \\ df &= \frac{U}{2\pi} dk_1\end{aligned}$$

Thereby

$$\sigma_i^2 = \int_0^{n_{max}U/z} S_i(f) df = \int_0^{\frac{2\pi}{z}n_{max}} S_i\left(\frac{U}{2\pi}k_1\right) \frac{U}{2\pi} dk_1 = \int_0^{k_{1,max}} F_i(k_1) dk_1$$

by use of the relations:

$$f = \frac{U}{2\pi}k_1; \quad f_{max} = \frac{U}{2\pi}k_{1,max}; \quad k_{1,max} = \frac{2\pi}{U}f_{max} = \frac{2\pi}{U}n_{max}U/z = \frac{2\pi}{z}n_{max}; \quad df = \frac{U}{2\pi}dk_1 \quad (4.9)$$

For instance, the Kaimal along-wind ( $u$ ) spectrum now becomes, in wave number space:

$$F_u(k_1) = u_*^2 \frac{z}{U} \frac{U}{2\pi} \frac{102}{\left(1 + 33\left(\frac{U}{2\pi}k_1\right)z/U\right)^{5/3}} = u_*^2 \frac{z}{2\pi} \frac{102}{\left(1 + 33\frac{k_1z}{2\pi}\right)^{5/3}} \left[\frac{m^3}{s^2}\right] \quad (4.10)$$

#### 4.2.2 Modelling the ZephIR's spatial filters due to averaging

Averaging associated with the Lorentzian optical probe volume. It was shown<sup>4</sup> that the horizontal variance as measured by an upwind-looking (Spinner-based) Continuous Wave LiDAR, can be calculated from a low-pass Lorentzian-filtered turbulence of the Horizontal wave number spectrum  $F_u(k_1)$ , viz.:

$$\overline{\langle u \rangle^2} = \int_{-\infty}^{\infty} F_u(k_1) e^{-2z_R k_1} dk_1 \quad (4.11)$$

That is, the LiDAR measured variance results from the Longitudinal turbulence spectrum low-pass filtered by an exponential filter with a cut-off wave number given by  $k_1 \approx 1/2z_R$ .

In standard constant azimuth ( $\varphi = 30^\circ$ ) LDA scanning mode, the ZephIR LiDAR measures a combination of the ( $u, v, w$ ) velocity components. If we assume that the boundary layer turbulence is approximately isotropic on the limited scale of the Lorentzian filters HWHM parameter  $z_R$ , we can assume that the Lorentzian filter applies to all three velocity components, so we can define:

The Lorentzian optical probe volume is given by:

$$L_{Lorentzian}(k_1) = e^{-2z_R k_1} \quad (4.12)$$

2.2 Averaging associated with the three-revolution 3-s horizontal azimuth scans:

---

<sup>4</sup> In the note "Turbulence inside the ZephIR's measurement volume" Version tm\_02.doc; 06-03-2007, author: Torben Mikkelsen, VEA; Risø.

A simple model can be made if we assume that the resulting 3-second averaged wind vector is obtained from an average of the stream wise wind component over the area covered by three revolutions:

An effective instantaneous horizontal averaging length scale can be estimated as the combined result of time lag and the circular coverage, which for the ZephIR LiDAR is equal to the scan diameter (The ZephIR LiDAR scans a horizontal circle of diameter  $D$

equal to  $\frac{1}{\cos(30)} = \frac{2}{\sqrt{3}}$  times the measurement height, i.e. ( $D \approx 1.15z$ ). For

example, at a measuring height of 100 meters, the LiDAR beam rotates at a speed of  $\pi D \approx 363 \text{ [ms}^{-1}\text{]}$ . With the ZephIR's inherent spectral sampling frequency of 200.000 samples per second, it corresponds to an azimuthal displacement of the laser beam of  $\sim 1.81 \text{ mm}$  between two consecutive raw-spectral estimates. The ZephIR then averages such 4000 spectra during ( $5\mu\text{s} \times 4000$  averages), i.e. in  $\sim 20$  milliseconds (50 Hz) over an azimuth distance corresponding to  $1.81 \text{ mm}$  times 4000scans equal to an azimuthal conical segment of  $\sim 7.26$  meters.

In addition, the scan area covers a horizontal length scale given by the advection of the wind field by the mean wind speed during the ZephIR sampling time (3 s), see Fig. 4.3:

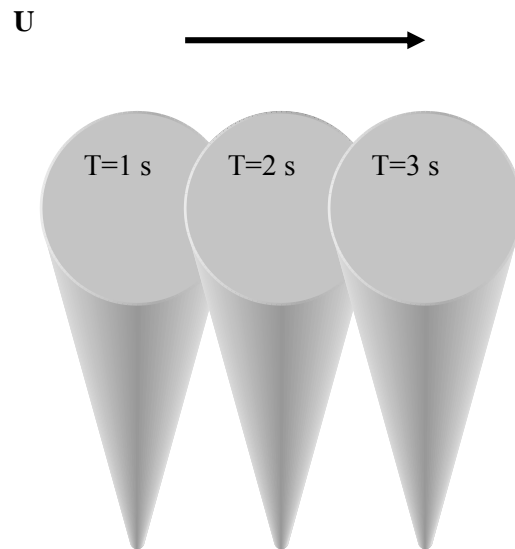


*Fig.4.3 The measurement area covered by the ZephIR LiDAR after three complete  $2\pi$ -azimuth scans, one per second, in a flow with mean wind speed  $U$ .*

Therefore, a simple effective horizontal length scale,  $l_{az}$ , representing an effective filter-averaging length scale from sampling over three consecutive perpetual revolutions ( $6\pi$  azimuth), can to a first approximation be modelled by:

$$l_{az} = D + U\Delta T = \frac{1}{\cos(30)} z + 3U = \frac{2}{\sqrt{3}} z + 3U \quad (4.13)$$

If we model the effect of the 3-sec lasting three-revolution azimuth scanning with a “Box car-like” filter function, we can further assume that the corresponding *Sinc* filter function ( $\frac{\sin^2 x}{x^2}$ ) applies as a low-pass filter on the turbulence in wave-number space, so that the combined 3-s  $6\pi$  azimuth filter function becomes

$$L_{AzimuthScan}(k_1) = \frac{\sin^2(\pi k_1 l_{az})}{(\pi k_1 l_{az})^2} \quad (4.14)$$

### 4.3 The Effect on ZephIR LiDAR measurements:

With the above defined filters, we next investigate the combined Lorentz-filter and 3-s sampling effect on the stream wise variance. For comparison with mast-mounted sonic anemometer measured variances, we first calculate the stream wise wind speed variance of the 3-sec averaged horizontal wind speeds, measured by the LiDAR (Lorentz- and Azimuth averaged), as :

$$\langle u'^2 \rangle_{ZephIR} = \int_0^{\infty} F_u(k_1) L_A(k_1) L_L(k_1) dk_1$$

with

$$L_L(k_1) = e^{-2z_R k_1}, \quad L_A(k_1) = \frac{\sin^2(\pi k_1 l_{az})}{(\pi k_1 l_{az})^2}$$

where

$$F_u(k_1) = u_*^2 \frac{z}{2\pi} \frac{102}{(1 + 33 \frac{k_1 z}{2\pi})^{5/3}} \left[ \frac{m^3}{s^2} \right]$$

and

$$l_{as} = \frac{2}{\sqrt{3}} z + 3U \text{ and } z_R(z) \approx 0.00085 \left( \frac{2}{\sqrt{3}} z \right)^2 = 0.00113 z^2 [m]$$

For the vertical wind speed profile we will assume typical danish Høvsøre Test Site parameters:

$$\text{Roughness } z_0 = 0.001[m]; \text{ Friction velocity } u_* = 0.5[ms^{-1}]; U(z) = \frac{u_*}{0.4} \ln \frac{z}{z_0} \Rightarrow U(100) \sim 15 ms^{-1}. \quad (4.15)$$

The LiDAR-filtered turbulence variance for the horizontal turbulence component Eqs(4.15) has been evaluated using Mathematica, cf. Fig.4.4. Corresponding expressions for the lateral and vertical components are shown in Fig. 4.5-4.6.:

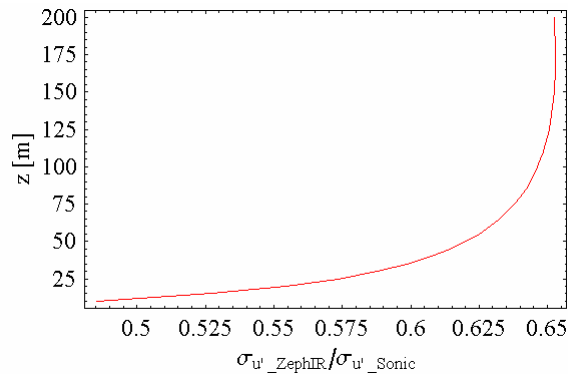


Fig. 4.4 Kaimal-modeled ZephIR stream wise wind speed standard deviations (inferred from consecutive three  $\times 2\pi$  azimuth scans), relative to unfiltered (Sonic) values, as function of measurement height.

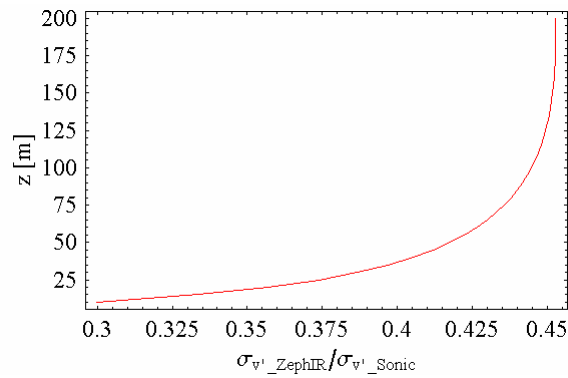


Fig. 4.5 Predicted ZephIR lateral wind speed standard deviations (inferred from consecutive three  $\times 2\pi$  azimuth scans), relative to unfiltered (Sonic) values, as function of measurement height.

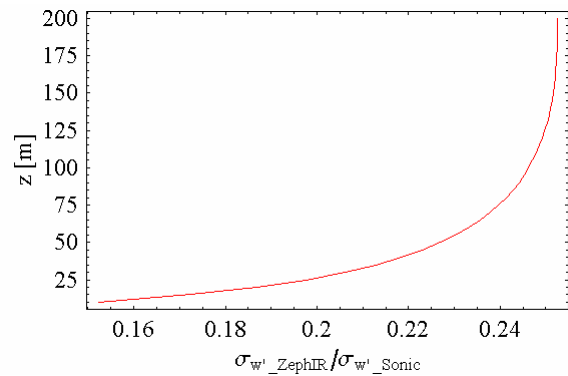


Fig. 4.6 Predicted ZephIR vertical wind speed standard deviations (inferred from consecutive three  $\times 2\pi$  azimuth scans), relative to unfiltered (Sonic) values, as function of measurement height.

#### 4.3.1 Conclusion on measured turbulence level

Our spectral filter model of the QinetiQ ZephIR measured turbulence levels predicts, that the QinetiQ ZephIR configured LiDAR measured variance at e.g. 100 meters height, compared to a sonic anemometer measurements, will be reduced by:

- ~ 37% in the along wind direction (cf. cup anemometer measurements)
- ~ 52% for the transversal wind component, and
- ~ 75 % for the vertical wind component.

#### 4.4 The filter effects on the ZephIR measured “TQE”

In the note “TQE & Shear stress\_Tensor\_from\_QQZephIR.doc”, it was shown that the ZephIR LiDAR measured “turbulence parameter” could be compared to the standard expression for Turbulent Kinetic Energy, TKE, defined as

$$TKE = \frac{1}{2} \left( \langle u^2 \rangle + \langle v^2 \rangle + \langle w^2 \rangle \right) \quad (4.16)$$

but with the following modifications:

By use of 25% of the full  $\langle u^2 \rangle$  variance; 25% of the full  $\langle v^2 \rangle$  variance, and 150% of the full  $\langle w^2 \rangle$  variance, the QinetiQ ZephIR LiDAR’s internal calculated “Turbulence parameter” was shown to be identical with a turbulence intensity based on the following definition of “Total “QinetiQ Eenergy””:

$$TQE \equiv \frac{1}{2} \left( \frac{1}{4} \langle u^2 \rangle + \frac{1}{4} \langle v^2 \rangle + \frac{3}{2} \langle w^2 \rangle \right) \quad (4.17)$$

Based on the Kaimal spectra variance estimations in Eqs (4.6) we find

$$TKE \square 4.43 u_*^2; \quad TQE \square 2.06 u_*^2, \quad \text{and} \quad \frac{TQE}{TKE} \square 0.46 \quad (4.18)$$

The definition of TQE in Eqs. (4.17) is defined in terms of “un-filtered” variances, that is, with no effects of the LiDAR’s spatial and temporal averaging considered.

To investigate and evaluate the averaging effects of ZephIR measured turbulence, we next re-calculate the variances in eqs. (4.17) including the filter effects.

Define the filter-averaged Total QinetiQ Energy in terms of ZephIR measured space and time averaged variances as

$$TQE_{av} \equiv \frac{1}{2} \left( \frac{1}{4} \langle u^2 \rangle_{av} + \frac{1}{4} \langle v^2 \rangle_{av} + \frac{3}{2} \langle w^2 \rangle_{av} \right) \quad (4.19)$$

Where we as above calculate the ZephIR averaged variances by filtering, viz.:

$$\langle u \rangle_{av}^2 = \int_0^{\infty} F_u(k_1) L_A(k_1) L_L(k_1) dk_1$$

$$\langle v \rangle_{av}^2 = \int_0^{\infty} F_v(k_1) L_A(k_1) L_L(k_1) dk_1$$

$$\langle w \rangle_{av}^2 = \int_0^{\infty} F_w(k_1) L_A(k_1) L_L(k_1) dk_1$$

where:  $L_L(k_1) = e^{-2z_R k_1}$ ;  $L_A(k_1) = \frac{\sin^2(\pi k_1 l_{az})}{(\pi k_1 l_{az})^2}$

and with standard Káimál power spectra (in wavenumber presentation) given by

$$F_u(k_1) = u_*^2 \frac{z}{2\pi} \frac{102}{\left(1 + 33 \frac{k_1 z}{2\pi}\right)^{5/3}} \left[ \frac{m^3}{s^2} \right]$$

$$F_v(k_1) = u_*^2 \frac{z}{2\pi} \frac{17}{\left(1 + 9.5 \frac{k_1 z}{2\pi}\right)^{5/3}} \left[ \frac{m^3}{s^2} \right]$$

$$F_w(k_1) = u_*^2 \frac{z}{2\pi} \frac{2.1}{1 + 5.3 \left(\frac{k_1 z}{2\pi}\right)^{5/3}} \left[ \frac{m^3}{s^2} \right]$$

As before:  $l_{as} = \frac{2}{\sqrt{3}} z + 3U(z)$  and  $z_R(z) \square 0.0016 z^2 [m]$ .  
(4.20)

Results are graphed in figs. 4.7 to 4.9.

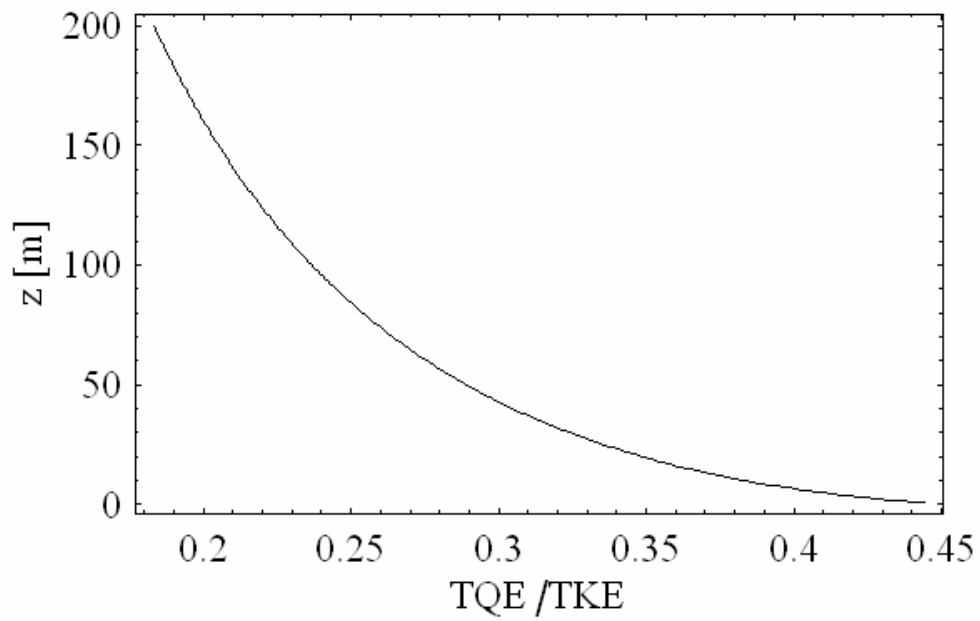


Fig 4.7. Prediction of ZephIR sampled TQE turbulence relative to unfiltered (Sonic) variance TKE, as function of measurement height. (Averaging time corresponding to 10-min).

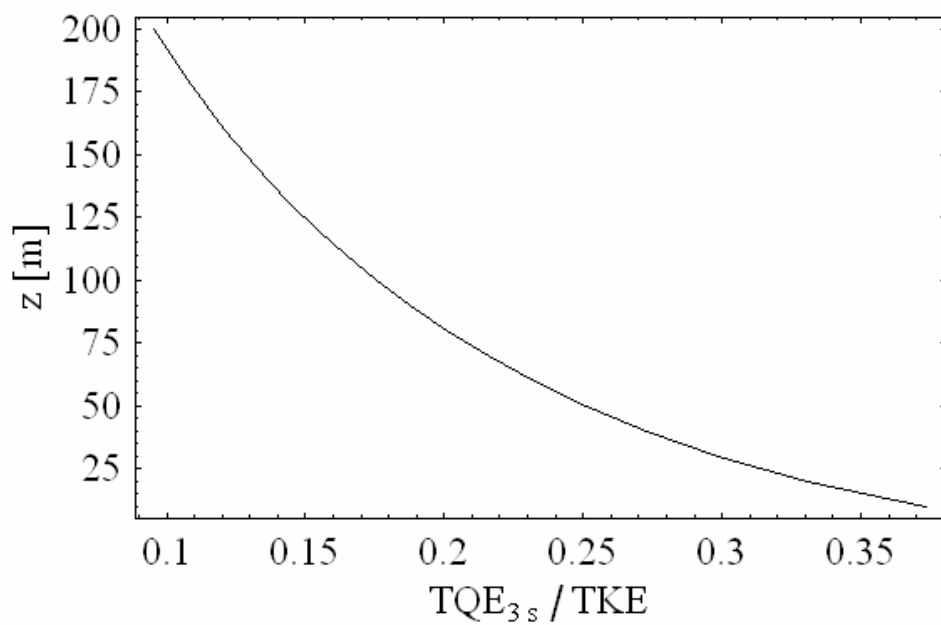
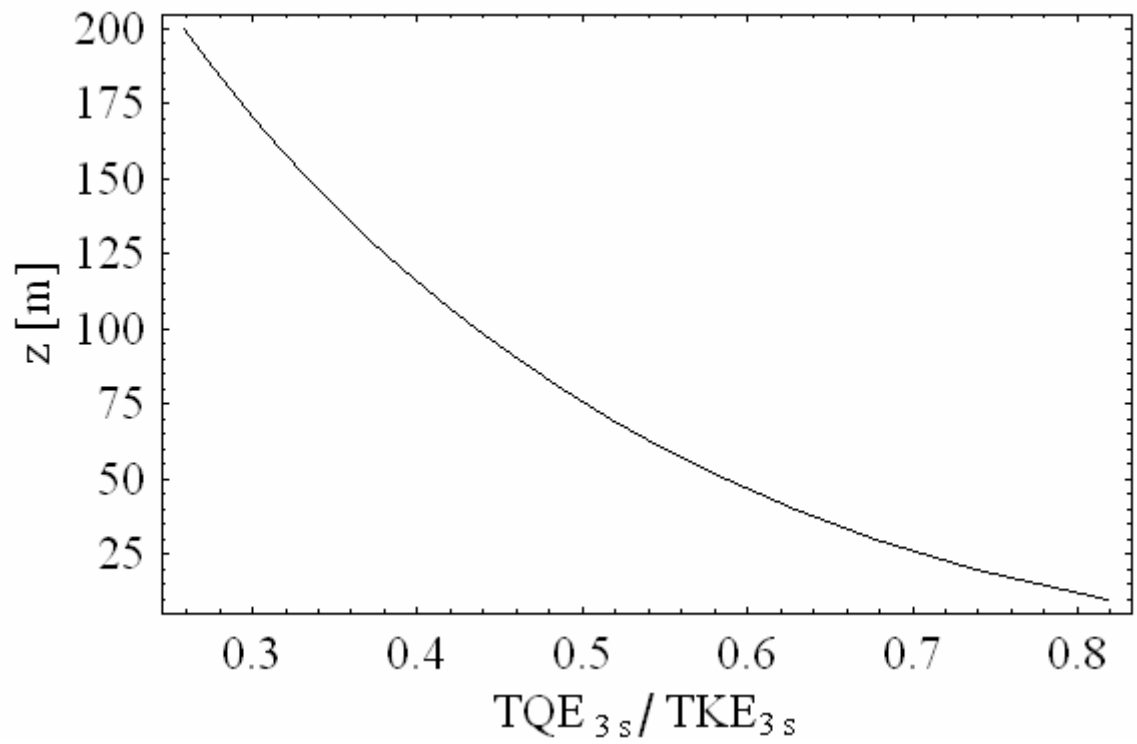


Fig 4.8. Prediction of 3-sec averaged TQE turbulence relative to unfiltered (Sonic) variance TKE, as function of measurement height.



*Fig 4.9. Prediction of 3-sec averaged  $TQE_{3s}$  turbulence, relative to 3-s averaged (Sonic) turbulence  $TKE_{3s}$  as function of measurement height.*

## 5 A generic description of the SODAR instrument (up to 300 m)

*Ioannis Antoniou*

SODARs send and receive successive pulses of sound in a number of beam directions, generally including a vertical beam and several beams tilted at small angles to the vertical. At least three beams in differing directions are needed in order to obtain measurements of the 3D wind velocity. When one of these sound pulses is transmitted, sound is scattered by turbulent refractive index changes at all heights, and acoustic energy scattered back to the ground is collected by microphones. Usually the speakers which transmit the pulse are also used as microphones, thus ensuring a compact acoustic antenna. This process gives a continuous time record of echo strength related to turbulent intensity. Knowledge of the local speed of sound,  $c$ , allows the time,  $t$ , elapsed since transmitting to be interpreted in terms of the height,  $z$ , from which an echo originated using:

$$z = \frac{ct}{2} \quad (5.1)$$

The result is a height profile of a measure of turbulent intensity.

If the scattering turbulence has a component of motion parallel to the beam direction, this changes the acoustic frequency of the echo ('Doppler shift'). Analysis of the frequency spectrum of the received back-scattered signal allows estimation of the speed of the turbulence parallel to the beam as a function of height.

Some seconds after the pulse is transmitted the echo signals are too weak to be detected above the background electrical and acoustic noise, because of spherical spreading of the energy and also atmospheric absorption. At this time the next acoustic pulse is transmitted, generally in a different direction so that a different component of the wind is estimated. Because of the conical beam shape, the volume occupied by the transmitted acoustic pulse increases as it progresses vertically; the echo from height  $z$  is received after travelling distance  $2z$ ; and a scattering layer of finite thickness lengthens the received signal. For an acoustic pulse duration of  $\tau$  and beam width  $\Delta\phi$ , the effective volume over which wind speed averaging takes place has vertical extent  $c\tau/2$  and horizontal radius  $z(\Delta\phi/2)$ , giving

$$V = \frac{c\tau}{2} \pi \left( \frac{z\Delta\phi}{2} \right)^2. \quad (5.2)$$

In practice it takes some time  $T$  to sample the echo signal for each frequency spectrum, and this time may be dominant in determining the averaging volume. In any case, it can be seen that the wind speed and direction estimates have a vertical spatial resolution which has a vertical extent determined by  $c\tau/2$  and  $cT/2$  and a horizontal spatial resolution of approximately  $z \Delta\phi/2$ . Since the various beams are generally tilted at angle  $\phi$  to the vertical, but in different directions, they are also horizontally separated by a distance of  $z\phi$  to  $2z\phi$  and this imposes some limitation because the separate wind components are not being estimated within the same volume.

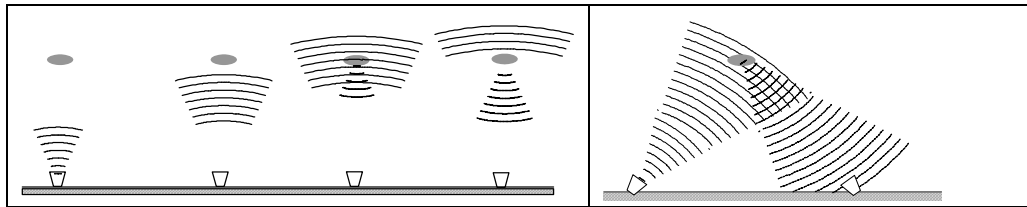


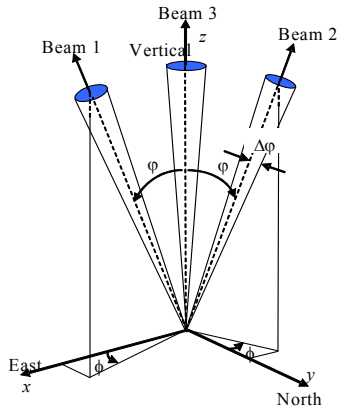
Figure 5.1 Principles of the monostatic and the bistatic SoDAR.

Throughout this text it is assumed that the speaker and microphone are the same. Such a SODAR configuration is called a monostatic SODAR. All commercial SODARs are monostatic. Advantages are that sender and receiver are not separated, which simplifies system design and reduces SODAR size. Disadvantages are that the scattering strength could be enhanced at scattering angles different from  $180^\circ$  (as in the case of bistatic SoDARs where transmitter and receiver are separated), reverberation of the system restricts the lowest measurement height, and the transmitted signal needs to be pulsed to allow height determination. The scattered sound power depicted by a SODAR is given by the following equation 5.3:

$$\sigma_s = \frac{1}{8} \frac{k^4}{k^3} \cos^2 \theta \left[ 0.033 \frac{C_T^2}{T^2} + 0.76 \cos^2 \left( \frac{\theta}{2} \right) \frac{C_V^2}{\pi c^2} \right] \quad (5.3)$$

where  $\theta$  is the scatter angle of return ( $180^\circ$ ),  $k$  is the wave number,  $T$  the ambient temperature, and  $C_T^2$  and  $C_V^2$  are the temperature and velocity structure functions respectively. The advantages of the bistatic relative to the monostatic design are obvious. The disadvantage of the bistatic arrangement is that it involves quite a lot of extra complexity to scan over different heights. As one of the biggest problems for SODAR measurements is poor signal-to-noise ratio (SNR), the added scattering strength due to velocity fluctuations measurable with bistatic SODARs may outweigh this disadvantage. The principles of the monostatic and the bistatic SODAR are shown in Figure 5.1. Both monostatic and bistatic systems can either use a horn driver and a parabolic dish or an array of speakers to produce a conical beam of sound.

The horn driver creates an almost spherical wave and if mounted above the focal point of a parabolic dish the reflected sound will ideally have the shape of an upward-directed parallel beam. In practice the shape will be conical and due to diffraction there will be side lobes which need to be attenuated by an absorbing surrounding wall called a baffle. Three dish antennas pointing in different directions are required to measure the wind vector. An array of speakers produces a similar beam pattern as the dish antenna. Due to sound interference between the different speakers the pattern tends to have narrower beams of higher power. Again a baffle is required to attenuate the side lobes. A SoDAR can have up to five beams with the 3-beam configuration as the most usual one. In Figure 10, a schematic presentation of the beams and the corresponding equations is given.



$$\begin{aligned}
 v_{r1} &= \underline{V} \cdot \underline{b}_1 = u \sin \varphi \cos \phi + v \sin \varphi \sin \phi + w \cos \varphi \\
 v_{r2} &= \underline{V} \cdot \underline{b}_2 = -u \sin \varphi \sin \phi + v \sin \varphi \cos \phi + w \cos \varphi \\
 v_{r3} &= \underline{V} \cdot \underline{b}_3 = w
 \end{aligned}$$

Figure 5.2 The principle for a three beam SoDAR.

The frequency content in the received signal includes electronic and background acoustic noise, Doppler shifted echo signals at frequencies near the transmitted frequency  $f_T$ , and echoes from nearby solid objects such as buildings or masts at the frequency  $f_r$ . The received signal is demodulated and sampled giving a Doppler FFT spectrum at discrete frequencies

$$f_i = i \frac{f_s}{N_f} \quad i = -\frac{N_f}{2} + 1, -\frac{N_f}{2} + 2, \dots, \frac{N_f}{2} - 1, \frac{N_f}{2} \quad (5.4)$$

where the spectrum contains  $N_f$  points sampled at a rate  $f_s$ . Each spectrum is therefore acquired over a time interval of  $T=N_f/f_s$  equivalent to a height interval of  $cN_f/2f_s$ . This height resolution for wind component estimation is typically  $\Delta z = 10$  m, giving spectral estimates separated by about  $\Delta f = 170/\Delta z = 17$  Hz. A transmitted pulse of duration  $\tau = 50$  ms gives a spectral peak of half width around 20 Hz, but the returned echo signal is accompanied by noise so a *peak detection* algorithm is required and the estimated Doppler shift frequency is subject to uncertainty. It is usual to average over perhaps 5 to 10 minutes to obtain an improved signal-to-noise ratio (SNR). This can be done by averaging the frequency spectrum obtained at each sampled height, or range gate, separately for each beam. Since noise is random and the echo signal not, an improvement by a factor  $\sqrt{N_s}$  is obtained in the SNR of the power spectrum if  $N_s$  spectra are averaged. Note however that the SNR may be considered too low in some cases and individual spectra excluded from the average, so that  $N_s$  may be different for each beam and each height over a particular averaging period. The radial velocity components give Doppler shifted echoes with frequency spectrum peaks at

$$\Delta f_j = -\frac{2v_{rj}}{c} f_r \quad j = 1, 2, 3, 4, 5 \quad (5.5)$$

Given the presence of noise, a peak detection algorithm is then used to determine the best estimate of  $\Delta f_j$  and hence solve the system for the wind components ( $u, v, w$ ). The SODAR incorporates signal-processing software to determine

- The position in the spectrum of the signal peak (corresponding to Doppler shift).
- The averages over a number of profiles (to improve SNR).

Among the common assumptions used for SODAR measurements are that

1. scatterers move with the mean flow
2. the scattering cross section is produced by frozen, homogeneous, and isotropic turbulence
3. turbulence and wind properties are the same in all sampled volumes at one particular height
4. vertical velocity is much smaller than horizontal velocities
5. beams are transmitted in a straight line (no beam bending due to wind drift)
6. the measurement volume is illuminated evenly by the transmitted pulse

In practice, small turbulent velocity deviations are detectable as a broadening of the spectral peak, but these deviations are sufficiently small that the basic scattering theory can be applied.

### **5.1 SoDAR calibration principles**

SODARs need to be calibrated before they are used for wind energy purposes. The reasons for this are connected to the influence of the atmospheric temperature on the speed of sound and other various stability situations encountered during the instrument's operation which are not considered adequately during the analysis of the results phase. Also a number of assumptions as described above play a decisive part in the deviations between cup and SoDAR measurements. Our experience from using the AQ500 SoDAR on onshore locations shows that the SoDAR underestimates the wind speed by an average of 5%.

Previous experiences using a SoDAR and cup measurements in flat terrain have resulted in a field calibration method. Using this method a low met mast (30-40m height) and a SoDAR are deployed close to each other. The SoDAR measurements are compared to the cup anemometer measurements for the mast height and the relation produced is used in order to calibrate the data at a higher height. The same data are used for the data filtering and the removal of the outliers and other spurious results at all heights of interest.

## 6 Mixing layer height theory

*Sven-Erik Gryning*

### 6.1 Boundary layer over the sea

The height of the boundary layer is a parameter that despite its obvious importance (Gryning et al, 1987; Gryning et al, 2007) is often unfairly treated or even neglected in experimental campaigns – this also holds for campaigns over the sea. Nevertheless it is an important meteorological parameter over the sea because the behaviour and characteristics of the marine boundary layer are quite different from the usual perception over land, the main difference being the profound influence of the waves on the turbulence and wind profiles.

The development of the marine boundary layer is very different in the coastal zone as compared to the open sea. While there is some understanding of the developments of the marine internal boundary layer in the coastal zone, the knowledge on the development of the boundary layer over the open sea is very limited and should be a research focus area in the future.

### 6.2 Measurements of the boundary layer height

The best way to estimate the height of the boundary layer is from profiles of turbulence, momentum and heat flux, but this is generally not possible because meteorological masts do not reach far enough into the boundary layer except under special conditions.

The traditional way of measuring the boundary layer height is by looking for kinks in profiles from radiosoundings; especially in the potential temperature, but also humidity and wind speed as well as the variability of the wind direction.

The use of a remote sensing for routine measurements of the boundary layer height is an interesting new challenge. The ceilometer is a new not yet fully explored instrument for boundary layer depth measurements. It is an inexpensive and sturdy instrument originally developed for routine cloud height observations, consisting of a vertically pointing laser and a receiver in the same location. It determines vertical aerosols profiles by measuring the time required for a pulse of light to be scattered back from the particles in the air. Assuming that particles within the boundary layer originate from the surface (land/sea) and that the particle concentration above the boundary layer is comparatively small, the height of the boundary layer can be determined from particle profiles measures by a ceilometer (figure 6.1).

This feature has been developed for research purposes. An example is from the Galathea3 expedition from April 2006 to August 2007 (figure 6.1). The the use of ceilometer needs to be investigated for operational purpose as well.



*Figure 6.1. Left panel shows the ceilometer (arrow) mounted on the research ship Galathea. Right panel shows the preparation of a radiosounding during the Galathea expedition.*

### **6.3 Marine boundary layer in the coastal zone.**

The discussion will be based on an experience from a two-week measuring campaign that was carried out in the fall of 1998 at Christiansø (Gryning and Batchvarova, 2002). The purpose of the campaign was to investigate the development of the boundary layer over the Baltic Sea. During the experiment the water was generally warmer than the air, which is a typical feature for the Baltic Sea during the late summer, autumn and early winter. This results in a generally positive sensible heat flux to the atmosphere, and the generation of a convectively driven boundary layer over the water.

Christiansø is marked with a cross in figure 6.2. For south-westerly winds (sector  $190^\circ$  to  $270^\circ$ ) Christiansø lies about 20 km downwind of Bornholm. For northerly winds (sector  $270^\circ$  to  $45^\circ$ ) the water fetch to the Swedish coast is about 100 km.

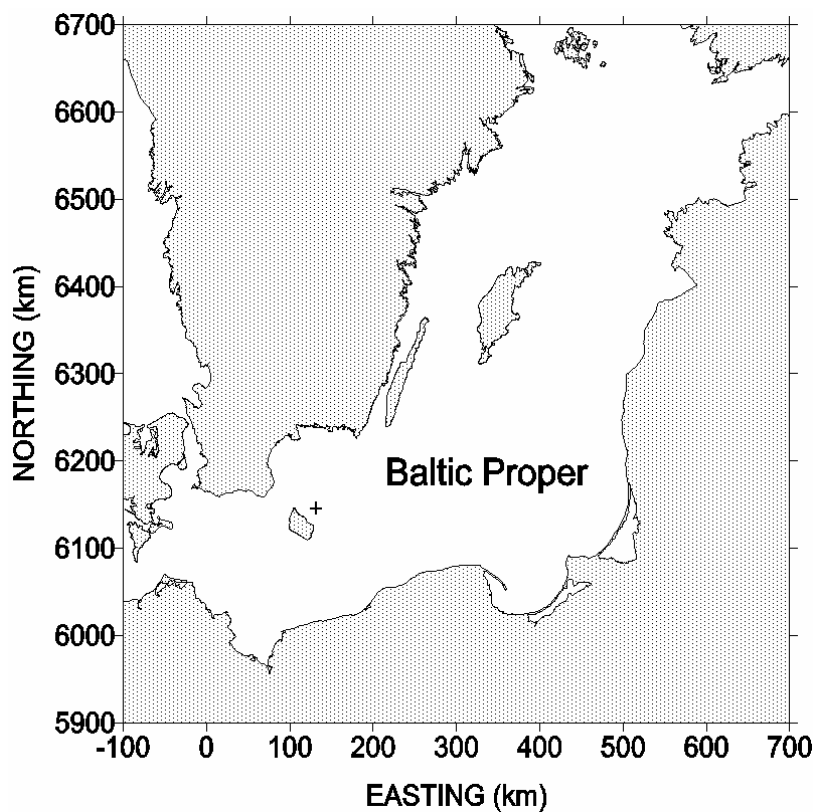


Figure 6.2. Map of the Baltic Proper with land surfaces and islands dotted. A cross shows the location of Christiansø east of Bornholm. The coordinate system refers to UTM34.

During an intensive observation period from 24 October to 5 November 1998 the depth of the boundary layer over Christiansø was estimated from frequently performed radiosoundings. For this experiment we additionally have output from simulations with the numerical weather prediction model HIRLAM.

The height of the boundary layer was simulated with a applied simple model (Gryning and Batchvarova 1996). The period from 26 October until midday 1 November 1998 is characterised by winds about  $12 \text{ m s}^{-1}$  from southwest to west. In this sector Christiansø is downwind of Bornholm with a water fetch of about 20 km. Following a wind direction shift on 1 November 1998 to northwest and north, the wind speed decreased to about  $4 \text{ m s}^{-1}$ . Then Christiansø is not downwind of Bornholm and the over water fetch from the Swedish coast is of about 100 km.

The right panel in figure 6.3 shows the evolution of the simulated boundary-layer height over Christiansø, when the marine internal boundary layer starts to develop at the eastern coastline of Bornholm. The overall agreement is fairly good.

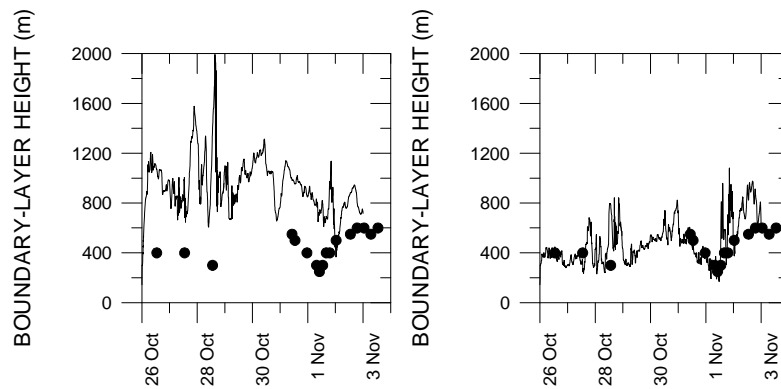


Figure 6.3. Simulations with the simple applied model of the evolution of the boundary-layer height over Christiansø during the extensive observation period. The solid line is the model simulation result and the bullets show the observations of the boundary-layer height from the radiosoundings. On the left panel Bornholm is not accounted for but it is replaced by water. On the right panel the effect of Bornholm is accounted for in the simulation.

The left panel similarly shows the evolution of the boundary-layer height but without accounting for the effect of Bornholm. Bornholm is here replaced by water. It can be seen that for the period up till noon on November 1, the simulated boundary layer is markedly higher than the measured one. Thereafter the agreement becomes better. Inspecting the wind direction reveals that up till November 1 around noon, the wind is within the sector that includes Bornholm, and then the wind turns towards north and the air that reaches Christiansø has not passed over Bornholm on its way but comes from the Swedish coast.

The model simulation suggests that the distance to the island of Bornholm during the first period controls the boundary layer over Christiansø, and during the second period it is the distance to the Swedish coast.

When simulations with Numerical Weather Prediction (NWP) or meso-scale models are available it is common practice to estimate the height of the boundary layer from the model output, and the simple applied model is usually not used. However, the height of the boundary layer does not form a part of the output from the meteorological models, but has to be derived from the available output data.

The High Resolution Limited Area Model HIRLAM is a complete model system for operational weather forecasts maintained by national meteorological services in Northern Europe. The horizontal grid resolution is 22.5 times 22.5 km and there are 31 vertical levels. Output from the simulations with the HIRLAM model includes hourly profiles of wind, temperature and humidity. Two methods to extract the boundary-layer height from the HIRLAM output data are applied and compared. Both are based on a bulk Richardson-number approach, but differ in the way the wind speed is taken into account. Starting from the lowest grid level the boundary-layer height is defined as the height,  $h$ , where the bulk Richardson number reaches a critical value.

Sørensen (1998) suggests the bulk Richardson number for the layer between the surface and the height  $z$  above the surface:

$$Ri_B = \frac{gz(\theta_v(z) - \theta_v(s))}{\theta_v(s)(u(z)^2 + v(z)^2)} \quad (6.1)$$

The quantities  $\theta_v(s)$  and  $\theta_v(z)$  are the virtual potential temperatures at the surface and height  $z$ , respectively,  $u(z)$  and  $v(z)$  are the horizontal wind components (easterly and northerly usually) as function of height. Vogelezang and Holtslag (1996) suggest a Richardson-number where the wind is defined with respect to the lowest model level (here 30-m), and a term that accounts for surface friction has been added

$$Ri_B = \frac{gz(\theta_v(z) - \theta_v(s))}{\theta_v(s)[(u(z) - u(s))^2 + (v(z) - v(s))^2 + bu_*^2]} \quad (6.2)$$

where  $b$  is a parameterisation constant recommended to be 100. Sørensen (1998) and Vogelezang and Holtslag (1996) made an empirical estimate on the value of the critical Richardson number. Despite their differences in the formulation of the bulk Richardson numbers both studies found a value of 0.25 for the critical Richardson number to be adequate.

The boundary-layer height deduced from HIRLAM output was compared to measurements of the marine atmospheric boundary layer that were carried out on Christiansø.

The result from the analysis using the Richardson number suggested by Sørensen (1998) is shown in the left panel on figure 6.4. It can be seen that the predicted boundary-layer height is clearly too high during the first part of the experimental campaign where the wind is southwesterly. When the wind turns towards north such that Bornholm no longer affects the air mass over Christiansø, agreement between measurements and predicted boundary-layer heights improves considerably. The right panel shows the results when using the Richardson number suggested by Vogelezang and Holtslag (1996). It can be seen that the predicted boundary-layer height generally is substantially lower than on the left panel, but still overpredicts the boundary-layer height for the first part of the simulation where the wind passes over Bornholm before reaching Christiansø. The agreement is better during the last part when the wind is northerly and the effect of Bornholm is absent.

The poor result in combination with good results from the simulation with the simple slab model suggests that the island of Bornholm controls the boundary layer over Christiansø during the first part of the period. The HIRLAM model grid is too coarse to resolve the effect of Bornholm.

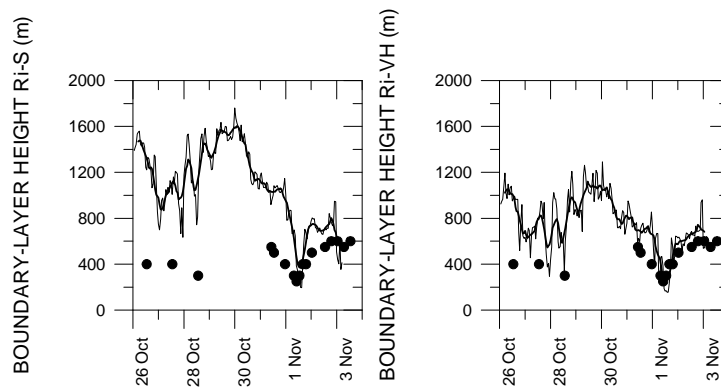


Figure 6.4. Boundary-layer heights over Christiansø during the extensive observation period, estimated from profiles of wind and temperature from the HIRLAM model, are shown by thin lines. The left panel shows the results using the Richardson number suggested by Sørensen (1998), the right panel when using the Richardson number in Vogelezang and Holtslag (1996). Bullets show the measurements. The thick line illustrates a running mean over 9 points.

During the last period of the experiment the wind was northerly. The air that reached Christiansø did not pass Bornholm on its way, but the water fetch to the nearest coast was about 100 km. For this case better agreement between measured and simulated boundary-layer heights was found for all the model simulations, indicating that for a water fetch of 100 km HIRLAM is able to resolve the change from land to sea.

The effect of the surface roughness on the critical Richardson number can be seen in the simulations of the boundary-layer height over Christiansø for long water fetches (westerly to northerly wind). Gryning and Batchvarova (2003) found the critical Richardson number that subjectively gave the overall best fit to the measurements to be 0.03 for the method suggested by Sørensen (1998) and 0.05 for Vogelezang and Holtslag (1996). This is illustrated in figure 6.5 where it also is evident that the Vogelezang and Holtslag (1996) method for this limited set of measurements gives a slightly better overall fit than Sørensen (1998).

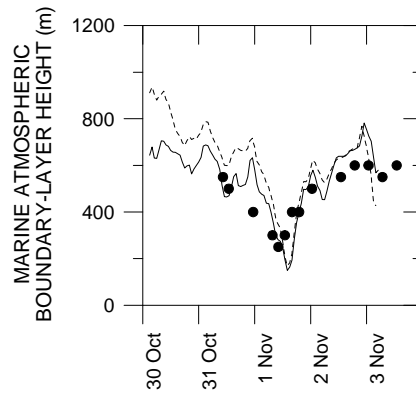
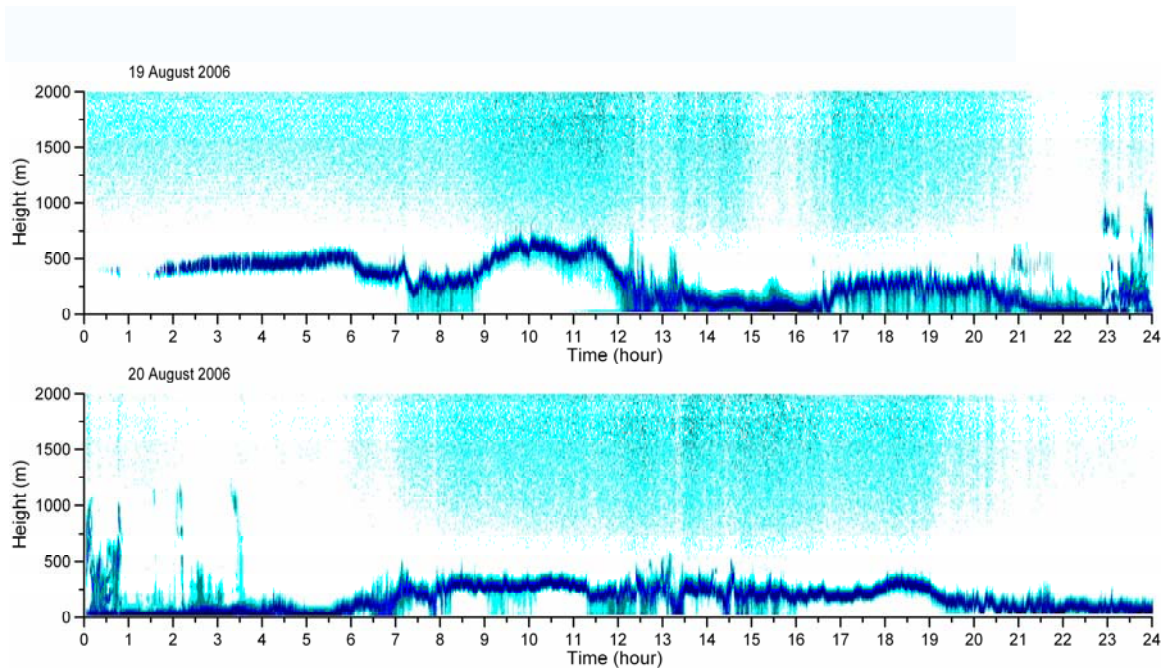


Figure 6.5 Height of the marine atmospheric boundary layer. The dashed line illustrates the boundary-layer height predicted by the method of Sørensen (1998) when applying a critical Richardson number of 0.03, the solid line shows the predictions of the Vogelezang and Holtslag (1996) with a critical Richardson number of 0.05. Bullets show measurements.

#### 6.4 The height of the marine boundary layer at open sea

Most oceanographic expeditions have carried out meteorological measurements, including radiosoundings, but the activity is mainly in support for the oceanographic research or for the study the air-sea exchange processes. The height of the marine boundary layer traditionally has not been the focus for the research. A prominent exception is the Danish Galathea expedition, <http://www.galathea.nu/>, where quite extensive meteorological measurements with specific aims of meteorological research were carried out. The instruments that were installed onboard the ship in the Galathea expedition included a ceilometer that successfully measured profiles of aerosols up to a height of several kilometers during the entire expedition. These can be used to determine the depth of the marine boundary layer. An example covering two days from the North Atlantic is shown in figure 6.6.



*Figure 6.6. Measurements of aerosols concentrations measured by the ceilometer onboard Galathea during two days in the North Atlantic. The colors indicate aerosol concentration such that darker colors signify larger concentrations. The top of the boundary layer is cloud topped and easily seen as a dark blue line.*

It can be seen that the boundary layer has a depth of about 400 meters during these days. It can also be seen that the daily variation which is a typical feature of the boundary layer over land is absent over the sea. The analysis of the measurements on the boundary layer from the Galathea expedition is in its infancy but the preliminary results shows that a value of about 400 meters seems to be typical for the conditions over the North Atlantic.

Another example, but far from typical for North Atlantic conditions, is shown in figure 6.7. The measurements were performed in the up welling zone west of Namibia. It can be seen that the marine boundary layer is shallow, having a depth of about 200 meters. Part of the time atmospheric waves forms on the top of the boundary layer. Obviously the sea-spray is confined to the boundary layer and do not penetrate up into the free atmosphere, constituting near ideal conditions for measurements of the depth of the boundary layer by use of a ceilometer.

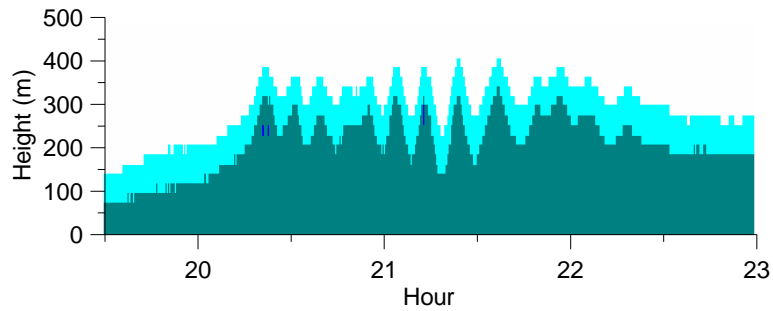


Figure 6.7. An example of boundary layer structure measured by the ceilometer during the Galathea expedition. The darker the colour the higher the particle concentration.

In the radiosoundings performed outside Namibia the top of the boundary layer is made known by an 15 deg increase of potential temperature and a simultaneous decrease of the wind speed from 11 to 3 m/s – ideal conditions for the formation of waves, figure 6.7.

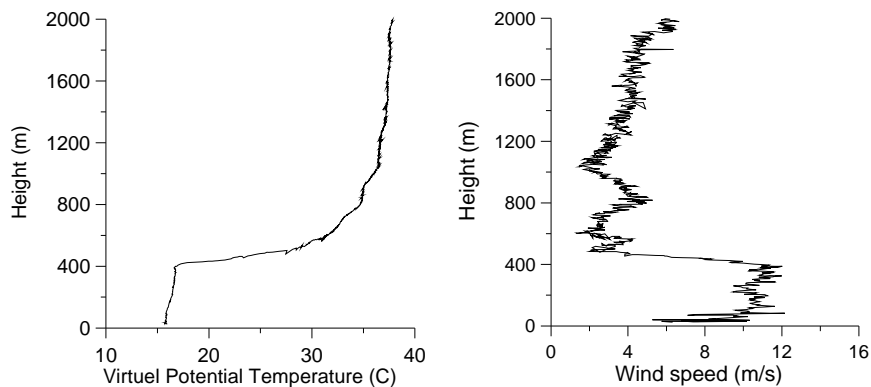


Figure 6.8. Radiosonde profiles from the event shown in figure 6.7.

## 6.5 Conclusions for mixing layer height theory

### 6.5.1 Coastal marine boundary layers

In an experimental campaign in the Baltic Sea the height of the marine boundary-layer height over Christiansø was found to be typically 500 m

The marine boundary-layer height over Christiansø varies on small and long time scales, but does not show the daily variation that is typical over land.

Bornholm influences the boundary-layer height over Christiansø for winds in the sector south to west where Christiansø lies downwind of Bornholm. The water fetch between Bornholm and Christiansø is about 20 km.

A simple applied, high resolution slab-type model of the boundary-layer height reproduced the characteristic behaviour of the boundary layer over Christiansø, both when Christiansø lies downwind of Bornholm with a water fetch of 20 km, and in northerly winds when Christiansø is downwind of the Swedish coast with a water fetch of 100 km or more.

The boundary-layer height was estimated from HIRLAM model output. Two methods were applied, both based on a Richardson-number approach. Both methods worked well for northerly winds, but both failed when Christiansø was downwind of Bornholm.

The grid resolution in the HIRLAM model is of the same size as the distance between Christiansø and Bornholm and the size of Bornholm itself. It is too coarse to reflect the mesoscale features that control the boundary-layer height over Christiansø when Christiansø is downwind of Bornholm. It seems to be adequate for northerly winds when Christiansø is downwind of the Swedish coast with a water fetch of 100 km or more.

### **6.5.2 Open sea boundary layers**

The knowledge on the formation and developments of the marine boundary layers over the open sea is scarce and insufficient and it should be a topic for future research initiatives.

During two days of the Galathea expedition the marine boundary-layer height over the open sea was found to vary on small and long time scales, but does not show the daily variation that is typical over land.

The marine boundary layer over the open sea was found to be about 400 meters in depth.

## 7 Results

Alfredo Peña

The analysis of the measurements performed with the ground-based remote sensing instruments on the platform and with the meteorological masts at Horns Rev is done by considering three main different inflow wind sectors (see Figure 7.1). These are:

- Open sea: This sector corresponds to wind coming mostly from the North-westerly sectors (directly from the open-sea).
- Land-influenced: This corresponds to the wind coming from the easterly sectors. The wind is directly influenced by the presence of the land (Jutland).
- Wake: This is wind influenced by the wind farm wake.

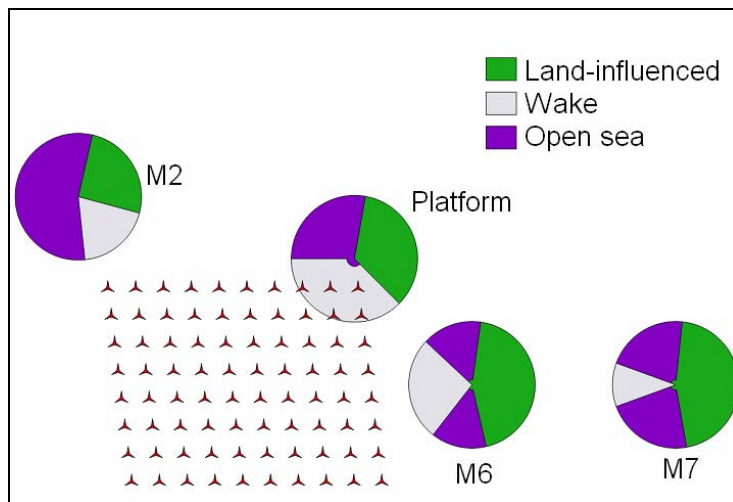


Figure 7.1. Different inflow sectors at the location of the masts and the platform in Horns Rev.

The direction of the different inflow sectors depends on the location in the wind farm as it is given in Table 7.1.

Table 7.1. Range of directions for the different inflow sectors at the locations in Horns Rev.

Location	Open sea [Deg.]	Land-influenced [Deg.]	Wake [Deg.]
M2	174 - 13°	13 - 105°	105 - 174°
M6	313 - 8° & 167 - 218°	8 - 167°	218 - 313°
M7	285 - 6° & 170 - 250°	6 - 170°	250 - 285°
Platform	270 - 10°	10 - 135°	135 - 270°

These three somewhat broad main inflow sectors were selected due to the different characteristics which the inflow wind has on the mean wind speed profiles as illustrated in Figure 4.16. The broad sectors help to increase the amount of profiles observed by both the ground-base sensing instruments and the cup anemometers on the masts.

The effect of the land is observed from the temperature observations at the masts. M2 has the largest fetch to land (approximately 20 km from Blåvandshuk) and the air temperature sensors registered the diurnal cycle for the easterly winds (Figure 7.2 (a)). This influence of land is not perceived from the westerly sectors (Figure 7.2 (b)).

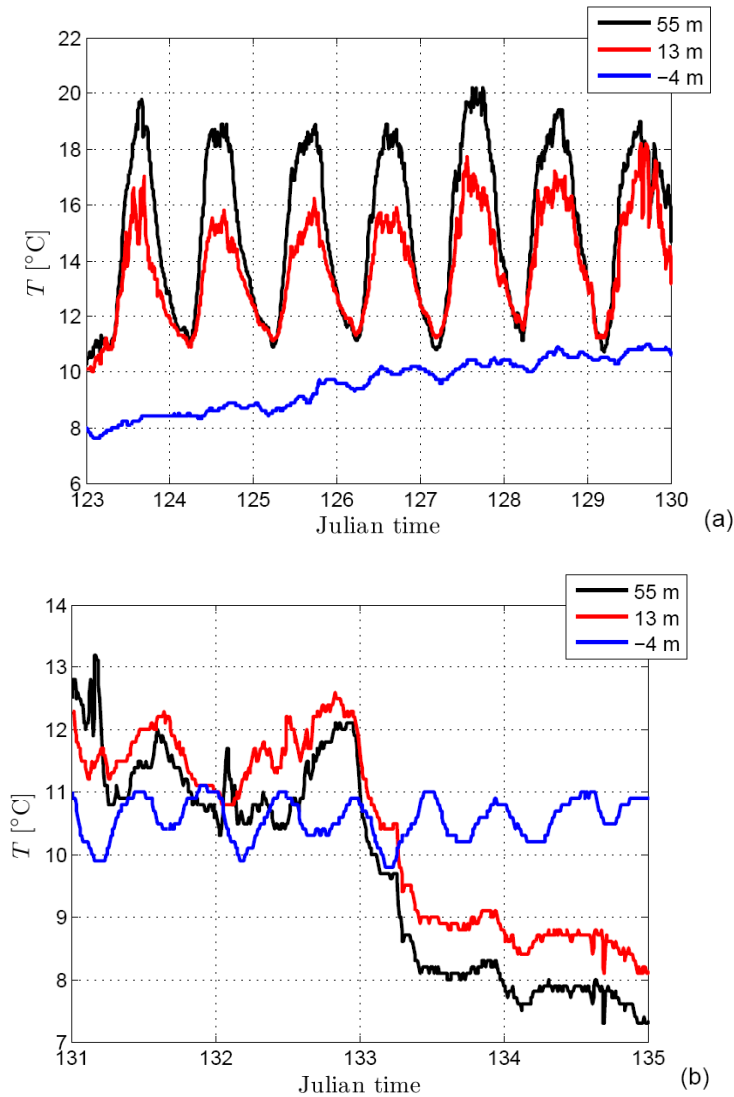


Figure 7.2. Temperatures at M2 registered at the air and water sensors. (a) For easterly winds (50 - 150°). (b) For westerly winds (210 - 360°).

## 7.1 Comparison results

The measurements of the LiDAR, the SoDAR and the cup anemometers at the masts were compared for their overlapping open sea sectors at similar heights. The wake and land-influenced sectors were excluded due to their inherent flow non homogeneities. Observations of horizontal mean wind speed below  $2 \text{ ms}^{-1}$  were also rejected for the study.

### 7.1.1 Mean wind speed

The correlation between 10 min horizontal mean wind speeds at three different levels is shown in Figure 7.3 for the LiDAR and the SoDAR measurements. The observations are normalized with the value of the highest observation value.

It is observed from figure 7.3 that the amount of data for each comparison decreases with height due to a low signal to noise ratio found in the SoDAR observations. This may be related to fixed echoes from reflections of different elements on the platform (e.g. a crane) or to the atmospheric conditions which were very close to neutral for most of the campaign's period. A continuous background noise from a sound alarm system used on the platform to scare birds could also be detected and this deteriorated the quality of the SoDAR data.

The analysis in the following is focused on the LiDAR data due to the low availability of the SoDAR measurements. A similar comparison is performed using the LiDAR observations and the measurements of the cup anemometers on the different masts at their overlapping heights. This is illustrated in Figure 7.4.

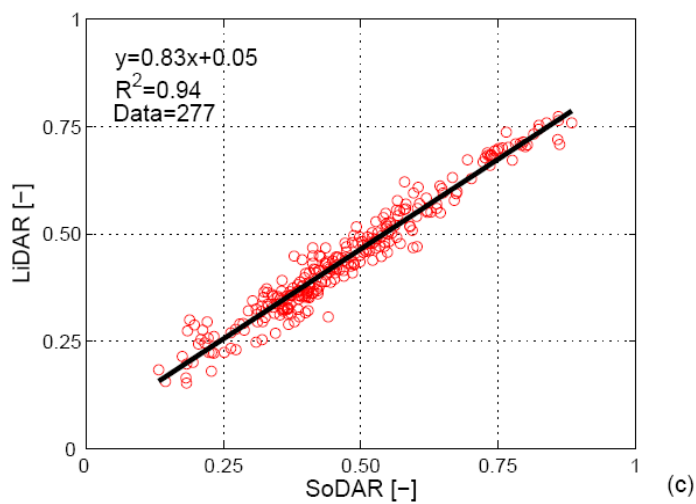
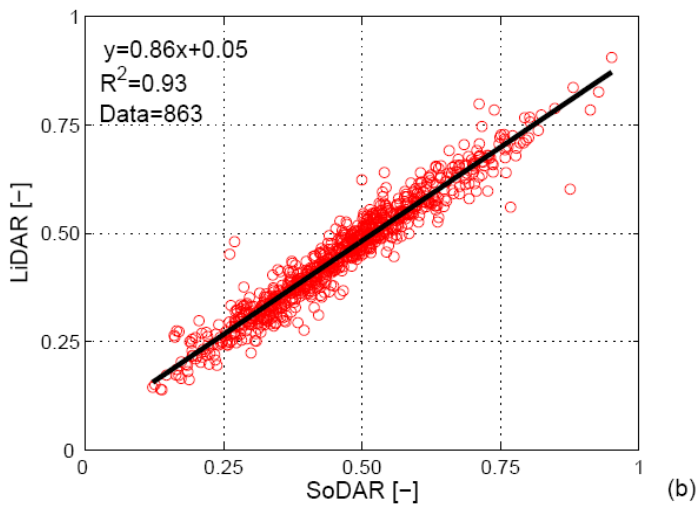
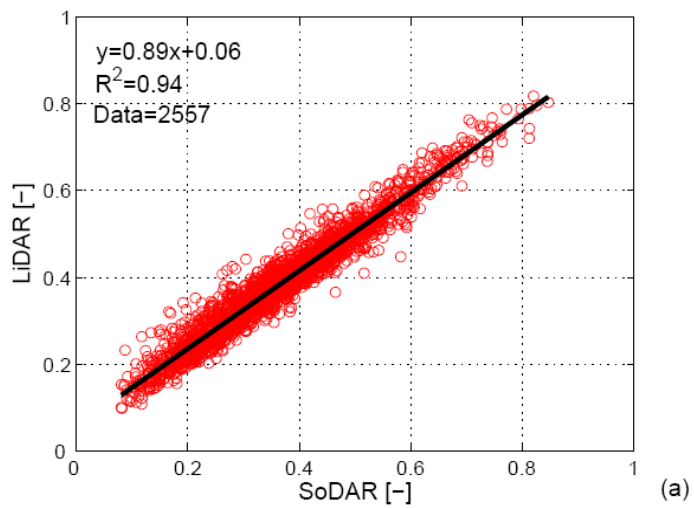


Figure 7.3. Comparison of normalized horizontal mean wind speed observed from the LiDAR and SoDAR. (a) LiDAR at 91 m and SoDAR at 95 m AMSL. (b) LiDAR at 121 m and SoDAR at 125 m AMSL. (c) LiDAR at 161 m and SoDAR at 155 m AMSL.

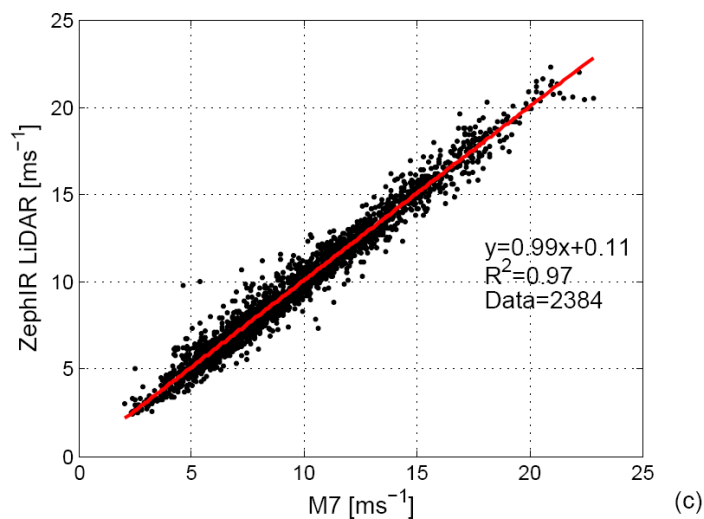
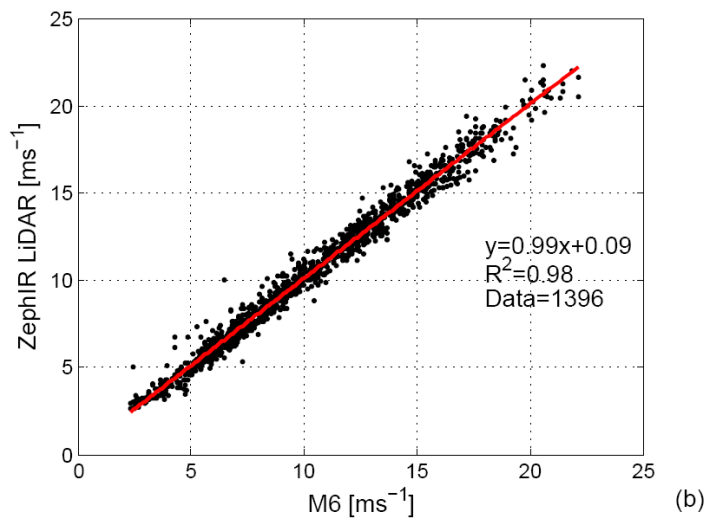
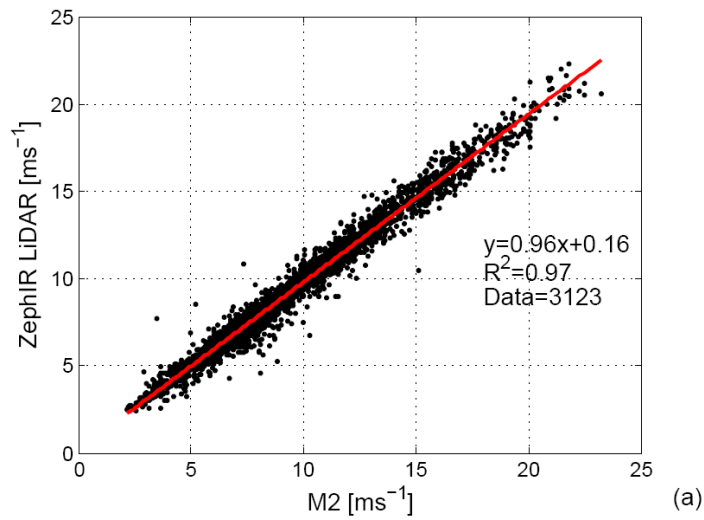


Figure 7.4. Comparison of horizontal mean wind speed observed from the LiDAR and the cup anemometers at the different masts. (a) LiDAR at 63 m and M2 at 62 m AMSL. (b) LiDAR at 63 m and M6 at 60 m AMSL. (c) LiDAR at 63 m and M7 at 60 m AMSL.

The correlation coefficients for all masts are high ( $\sim 0.98$ ) and the slopes of the linear regression are near unity. The comparison with M6 in Figure 7.4(b) shows the highest correlation and correspond to the closest mast to the platform. It is interesting to note that the comparison with M2 in Figure 7.4(a) is performed with the top-mounted cup anemometer which observes a higher wind speed for all the range of measurements. This can be related to the speed up effect previously mentioned when the wind speed profiles were analyzed for the cup anemometer observations in Figure 4.16.

### 7.1.2 Turbulence

Turbulence measurements of the standard deviation of the longitudinal component of the wind speed  $\sigma_u$  from the LiDAR were compared against turbulence measurements from the cup anemometers at the three masts. This is illustrated in Figure 7.4.

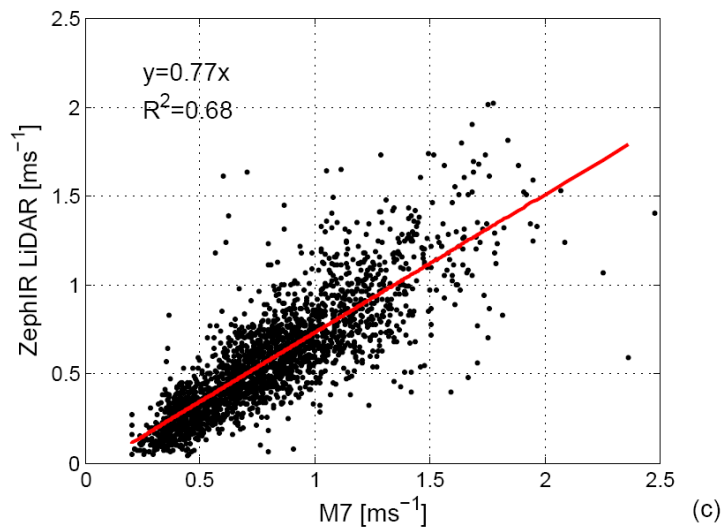
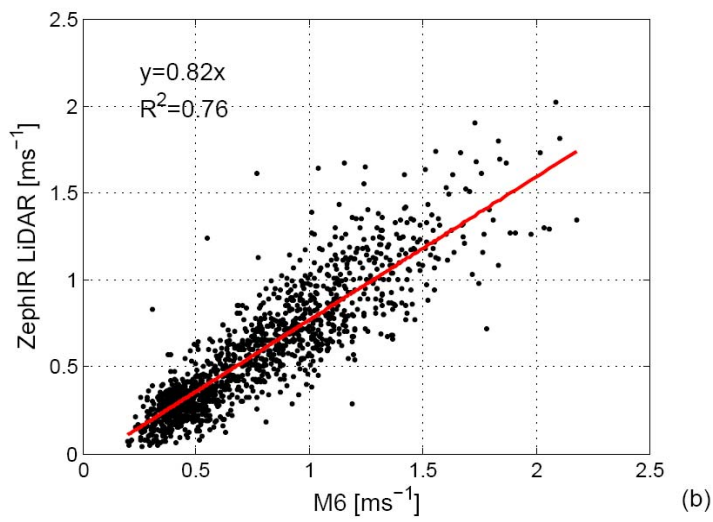
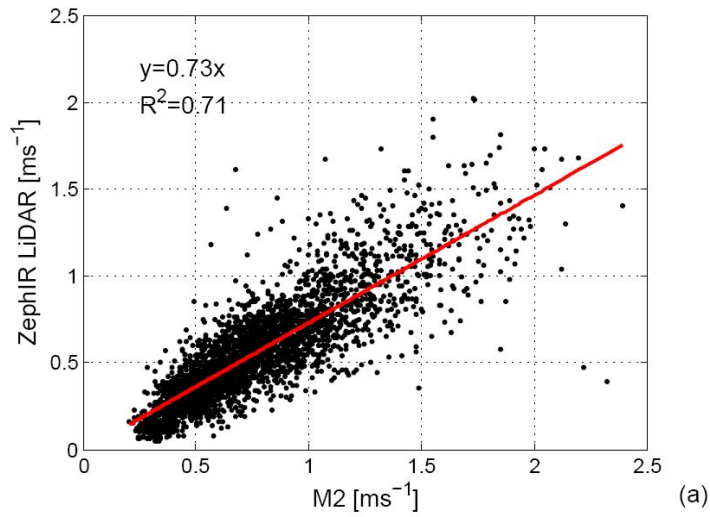


Figure 7.5. Comparison of  $\sigma_u$  from LiDAR against the cup anemometer observations. (a) LiDAR at 63 m and M2 at 62 m AMSL. (b) LiDAR at 63 m and M6 at 60 m AMSL. (c) LiDAR at 63 m and M7 at 60 m AMSL.

In figure 7.5, the correlations for the three different masts show good agreement especially for M6. From each linear regression it can be seen that the slope approximates a value around 0.8. This is due to the attenuation of the standard deviation observed by the LiDAR and explained in Section 5.1.1. The effect of the attenuation can be seen more clearly on the turbulence intensity which is given by:

$$I_u = \frac{\sigma_u}{\bar{u}} \quad (7.1)$$

where  $I_u$  is the longitudinal turbulence intensity and  $\bar{u}$  is the longitudinal wind speed (which is aligned with the wind direction and therefore corresponds to the horizontal mean wind speed). The general variation of the turbulence intensity with wind speed is known over land where the turbulence decreases as the wind speed is incremented. In Figure 7.6, this variation is illustrated for the measurements from a cup anemometer on M6 and the LiDAR observations.

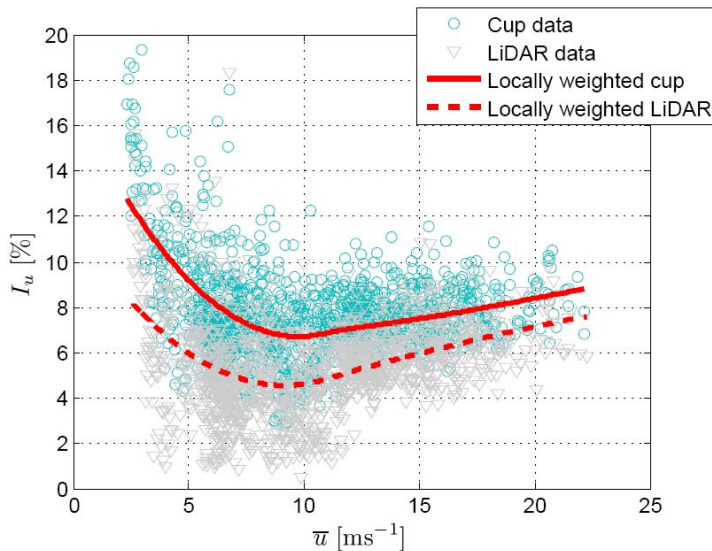


Figure 7.6. Variation of turbulence intensity with wind speed for the LiDAR observations at 63 m AMSL and the cup anemometer on M6 at 60 m AMSL.

It is illustrated in figure 7.6 that the turbulence intensity levels registered at Horns Rev for these open sea sectors are low. The area is characterized by a high degree of homogeneity due to the low roughness lengths of the sea. Observations from the LiDAR follow the behavior of observations from the cup anemometer: the turbulence decreases with wind speed up to  $10 \text{ ms}^{-1}$ . Beyond this level of wind speed, both LiDAR and cup anemometer turbulence intensities increase. This is due to the increase on the roughness length of sea at high wind speeds. The attenuation of the turbulence performed by the LiDAR is observed from the differences between the locally weighted curves<sup>5</sup> from the

<sup>5</sup> The locally weighted curve smoothes the data using a least squares quadratic polynomial fitting

cup anemometer and the LiDAR scatter plots. The figure shows that the degree of attenuation is dependant on the mean wind speed. The longitudinal standard deviation is attenuated around 20% at 60 m AMSL on the masts at Horns Rev.

In Figure 7.6 several locally weighted curves show the variation of turbulence intensity with normalized horizontal mean wind speed for the cup anemometers on M2 and for the LiDAR measurements at the different levels of observation.

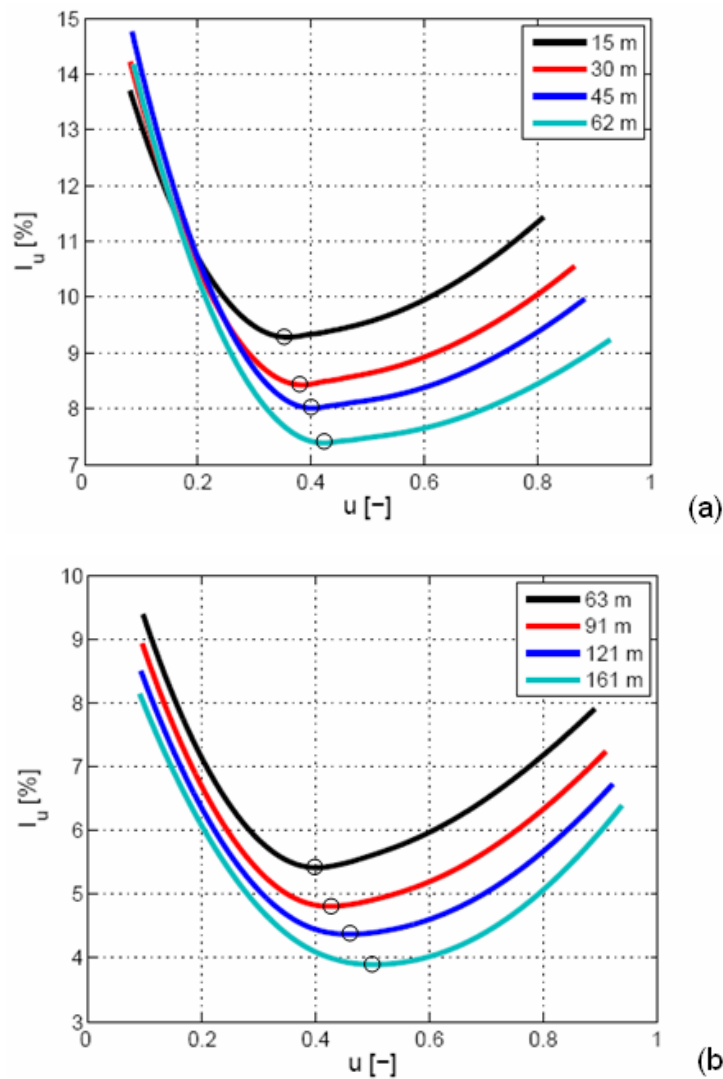
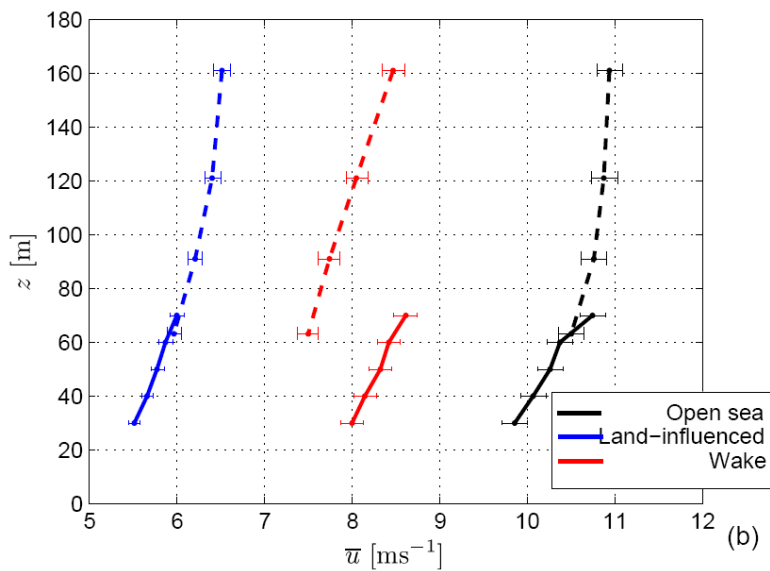
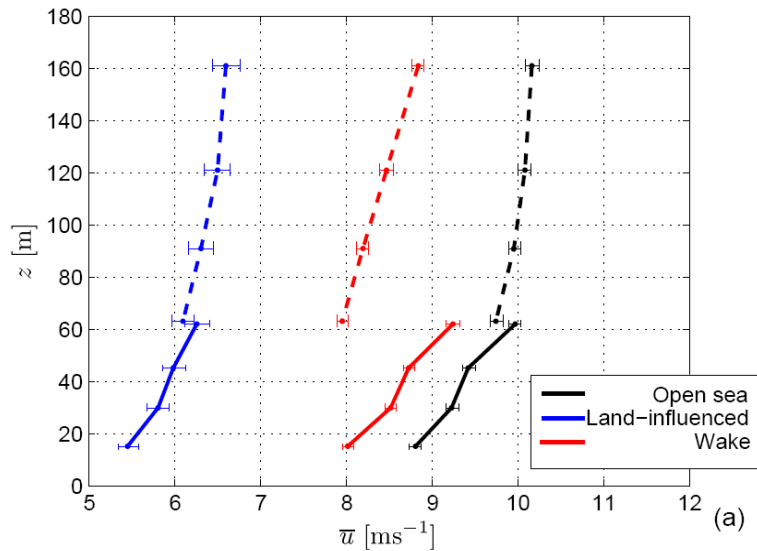


Figure 7.7. Variation of longitudinal turbulence intensity with normalized horizontal mean wind speed. (a) Observation at the cup anemometers at M2. (b) LiDAR observations.

The turbulence intensity levels clearly decrease with height. It is also illustrated in the figure that the range of wind speeds where the turbulence intensity increases, i.e. the lowest observation of turbulence in the curve, are moved to higher wind speeds as the observation is performed at higher levels. The effect of the increase of sea roughness length has a lower impact far from the sea surface.

## 7.2 Wind and turbulence profiles

The different individual 10 min profiles of horizontal mean wind speed are averaged on each of the overlapping platform/mast inflow sectors. The profiles of the cup anemometers are then extended up to 161 m AMSL using the LiDAR observations. This is illustrated in Figure 7.8 for the three masts.



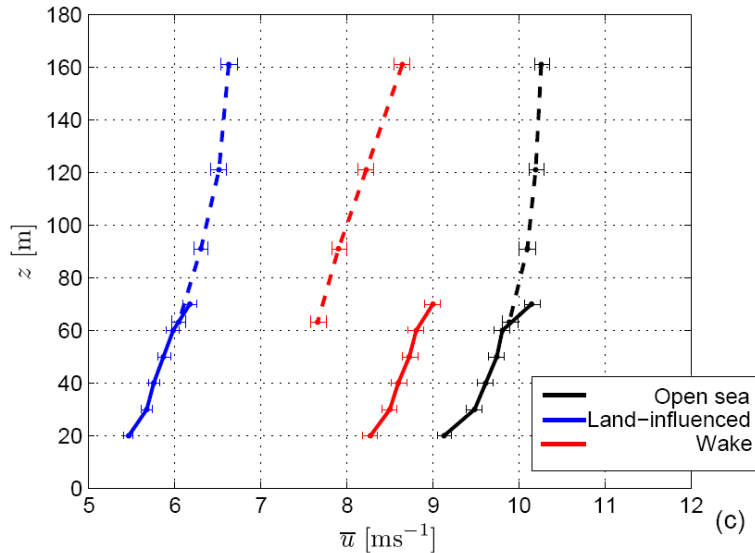


Figure 7.8. Extended horizontal mean wind speed profiles from cup anemometers are shown with LiDAR measurements. The dash lines correspond to LiDAR and solid lines to cup anemometers. (a). M2 and LiDAR. (b) M6 and LiDAR. (c) M7 and LiDAR. The +/- one standard error is indicated in the error bar.

The amount of data at each height is the same for the whole extended profile. The number of measured 10 min wind speed profiles on each inflow sector is given in Table 7.2.

Table 7.2. Number of measured profiles at the three different extended mast/platform conditions on each inflow sector.

Location	Open sea	Land-influenced	Wake
M2	2580	183	2177
M6	965	543	748
M7	1948	552	1450

Both the LiDAR and cup anemometer profile match well on the open sea and land-influenced sectors at all mast locations. The profiles do not match on the wake sector because the direction to the farm is different at each mast and platform location. The standard errors at the different levels are small.

The discontinuity in the wind speed profile at the top-mounted cup anemometer is also observed at all masts and the three inflow sectors. As it was illustrated in Figure 4.16, the difference between the top-mounted observation and the next low cup level is found to be bigger for higher mean wind speed. The LiDAR profiles in Figure 7.8 follow the low cup profiles. Observations from LiDAR do not suffer flow distortion or speed up as there is no mast structure (and the flow distortion due to the platform is assumed negligible for the selected observation heights). The results in figure 7.8 give evidence of a possible speed up on the top-mounted cups on the Horns Rev masts.

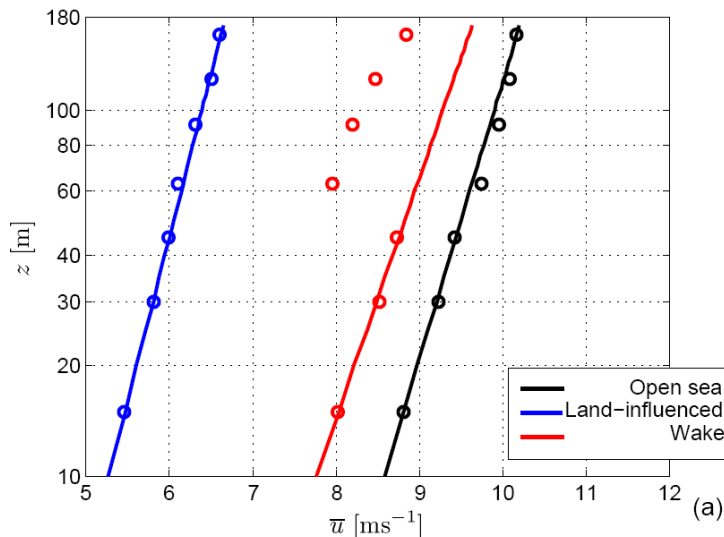
### 7.2.1 Modelling the offshore wind

The extended LiDAR/cup profiles are compared with the logarithmic wind profile which has been previously found to work well in the surface layer (e.g. in Gryning et. al, 2006 and Businger et. al, 1971) which corresponds to approximately the first 10% of the atmospheric boundary layer. This is given by:

$$\bar{u} = \frac{u_*}{\kappa} \ln\left(\frac{z}{z_o}\right) \quad (7.2)$$

where  $u^*$  is the velocity scale friction velocity in the surface layer,  $\kappa$  is the von Karman constant ( $\sim 0.4$ ),  $z$  is the height and  $z_o$  is the surface roughness length. The use of Eq. (7.2) implies that the roughness length corresponds to the height where the mean wind speed equals zero. Over the sea, this assumption is not valid and therefore, Eq. (7.2) should not be applied to the first couple of centimeters above the sea surface in the so-called wave boundary layer.

In the absence of measurements of turbulence fluxes, the friction velocity and the sea roughness lengths can be profile-derived from a minimum of two measurements of wind speed at different levels in the surface layer. This has been performed for the levels up to 45 m AMSL on M2 and 50 m AMSL on M6 and M7. The comparison between the measurements and the predicted mean wind speed from Eq. (7.2) is illustrated in Figure 7.9. The measurement of the top-mounted cup anemometers has been skipped for the analysis.



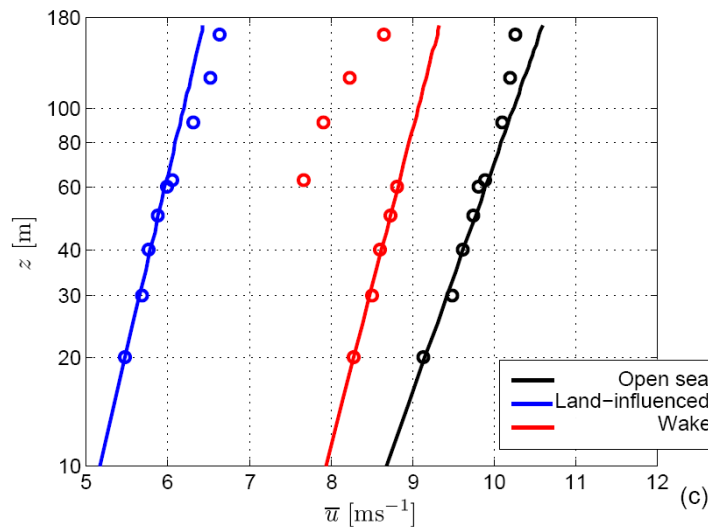
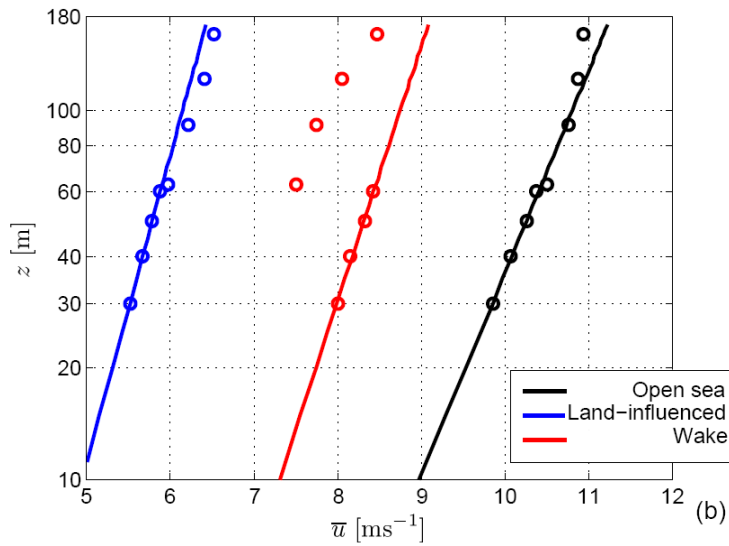


Figure 7.9. Comparison between the measurements and the predicted wind speed profiles from the logarithmic profile (solid lines). (a). M2 and LiDAR. (b) M6 and LiDAR. (c) M7 and LiDAR.

The deviations from the fitted profiles in figure 7.9 are small on the land-influenced and open sea inflow sectors at all masts. A small systematic over-prediction above 100 m for the open sea wind profiles at M6 and M7 can be noticed. These wind speed deficits may be related to the proximity to the land or the effect of atmospheric stability on the profile. The LiDAR measurements observe higher wind speeds on the land-influenced sectors at M6 and M7 because the fetch distance to the platform is larger than for both masts. The wake reference profiles are taken from the sectors where no wake is observed at each mast. Deficits of wind speed from the wind farm wake are observed at all heights measured by the LiDAR. In the most extreme case, i.e. where the highest wind speed deficit is observed at M7, the mean wind speed is decreased approximately 15% at the turbine's hub height.

## 7.2.2 The sea roughness length

The sea roughness length and the friction velocity were estimated in the previous section from the wind speed measurements applying Eq. (7.2). These estimations correspond to the average values over a broad range of sea state and atmospheric stability conditions. They can be compared with a model to account for the increase of the waves with wind speed. One of the most commonly applied, for the estimation of the sea roughness length, is the Charnock's relation (Charnock, 1955):

$$z_o = \frac{\alpha_c u_*^2}{g} \quad (7.3)$$

where  $\alpha_c$  is the Charnock's parameter ( $\sim 0.012$ ) and  $g$  is the gravitational acceleration. The comparison is illustrated in Figure 7.10 where the scatter represents individual 10 min estimations from the profiles which are close to neutral conditions. Eq. (7.2) is then assumed to be also valid for these individual profiles. The neutral conditions are approached using the bulk formulation of the drag coefficient (Kraus, 1972) which is given by:

$$\overline{w'T'} = C_z \overline{u_z} (T_o - T_z) \quad (7.4)$$

where  $z$  is a reference height (at 15, 30 and 20 m AMSL for M2, M6 and M7, respectively),  $\overline{w'T'}$  is the heat flux,  $C$  is the drag coefficient,  $T_o$  is the SST (Sea Surface Temperature) and  $T_z$  the air temperature (the closest to the observed cup anemometer at each mast). The value for the drag coefficient given by (Kraus, 1972) based on different observations is  $1.2 \times 10^{-3}$ ; thus given the interval  $\left| \overline{u_z} (T_o - T_z) \right| \leq 2$ , the absolute value of the heat flux is less than  $2.4 \times 10^{-3} \text{ Kms}^{-1}$ .

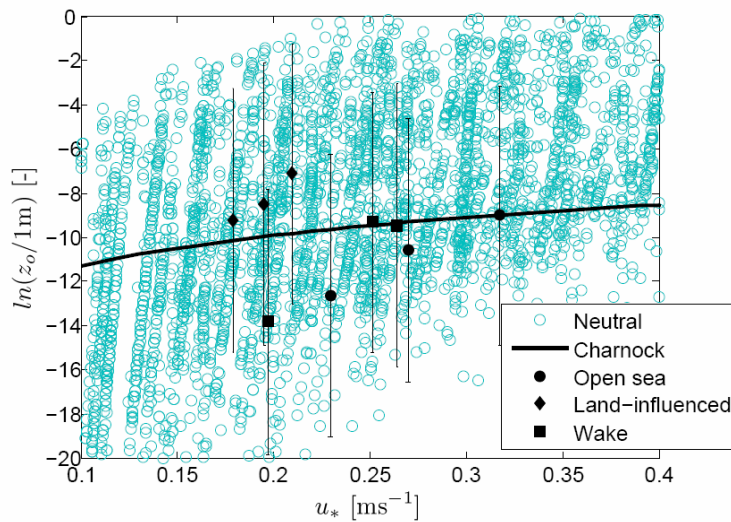


Figure 7.10. Comparison of profile-derived estimations of friction velocity and sea roughness length with the Charnock's relation (solid line). The variability of the profile-derived roughness length is indicated in the error bars when the estimation is performed from the higher and lower values of wind speed at the error bar tails in Figure 7.8.

The observed values of friction velocity are low and the roughness length estimations are high for all masts on the land-influenced inflow sector. This may be due to the influence of the land roughness on the wind profile. The estimations of roughness length are always higher than the Charnock's model which has been previously observed to work better for open sea than for coastal areas. It is interesting to notice that although the scatter of all individual estimations of roughness length is large, the profile-derived mean values are near the Charnock's model. In contrast with the friction velocity, the roughness length is a high sensitive parameter in Eq. (7.2). The Charnock's relation may be used to model the sea roughness in the logarithmic profile which results in an accurate wind speed prediction.

The temperature measurements at 4 m BMSL (Water) were used for the SST observations in Eq. (7.4). This assumption, at least for the period of the campaign, can be validated by comparison of these observations with the daily average SST observation from the satellite. This is illustrated in Figure 7.11 for M2.

Figure 7.11 shows the behavior of the air and sea temperature from the temperature sensors at the mast where the last follows closely the SST observation from the satellite (Høyer & She 2007). A linear regression is performed between the daily averaged SST from the satellite and the daily averaged 4 m BMSL water measurement from M2 in Figure 7.12.

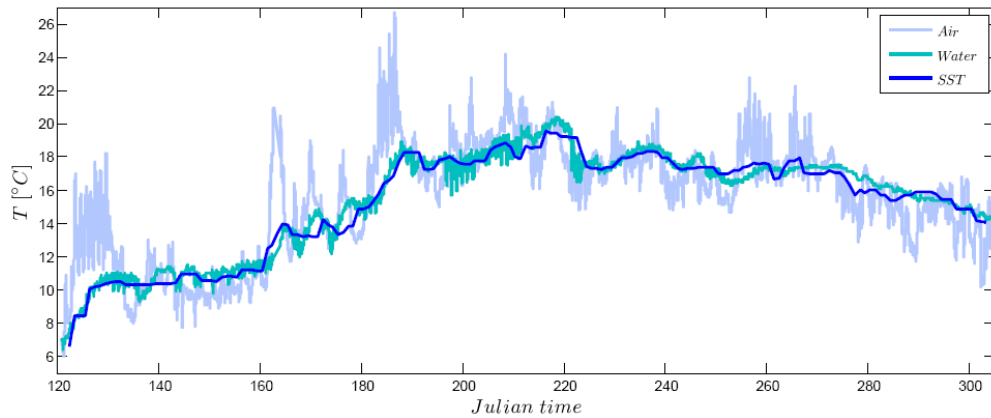


Figure 7.11. Comparison of observed temperatures at M2 with satellite SST measurements in 2006. The air temperature is taken at 55 m AMSL and the water at 4 m BMSL. SST data are courtesy of DMI.

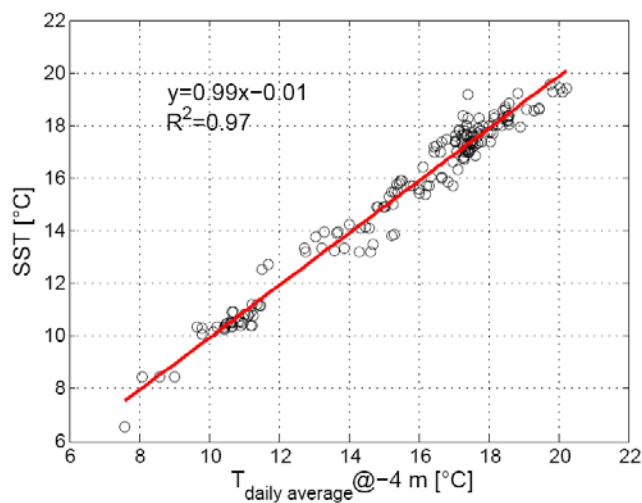


Figure 7.12. Comparison between the daily averaged measurements of SST from the satellite and the daily averaged observations at M2 at 4 m BMSL.

The correlation between both measurements is good, though the precision of the 4 m BMSL measurement is low (0.1 °C). For M6 and M7, the differences from the comparison are not much bigger. The resolution of the satellite SST observations gives spatial cells of 2x2 km.

### 7.2.3 Charnock's wind profiles

The Charnock's sea roughness model has been extended in the literature to include variables such as wave age (Smedman et al., 2003; Hara and Belcher, 2004), fetch distance (Lange et al., 2004), water depth (Larsén, 2003), wave height (Smedman et al., 2003), Reynolds number (Hara and Belcher, 2004), etc. but these parameters are normally difficult to measure. The simple Charnock's relation is then a useful tool for applied use. Högström et al. (2006) argued that the variation in the wind speed profile due to different roughness lengths is relatively small in the wind energy context based on

the logarithmic wind profile and the correction to account for atmospheric stability with the Businger-Dyer relations (Businger et. al 1971) and Monin-Obukhov similarity theory.

To illustrate the ability that the Charnock's model has on the prediction of the wind speed at different heights, the individual 10 min profiles on the LiDAR/mast overlapping open sea sector have been classified in five different wind speed ranges. An average wind speed profile is computed on each range of wind speeds using the lowest observation height as a reference. The friction velocity is estimated, as it was performed previously (see Figure 7.9), from the logarithmic profile where the sea roughness length is modeled using Charnock's relation. The results of these predicted Charnock's wind profiles and the averaged measurements are shown in Figure 7.13.

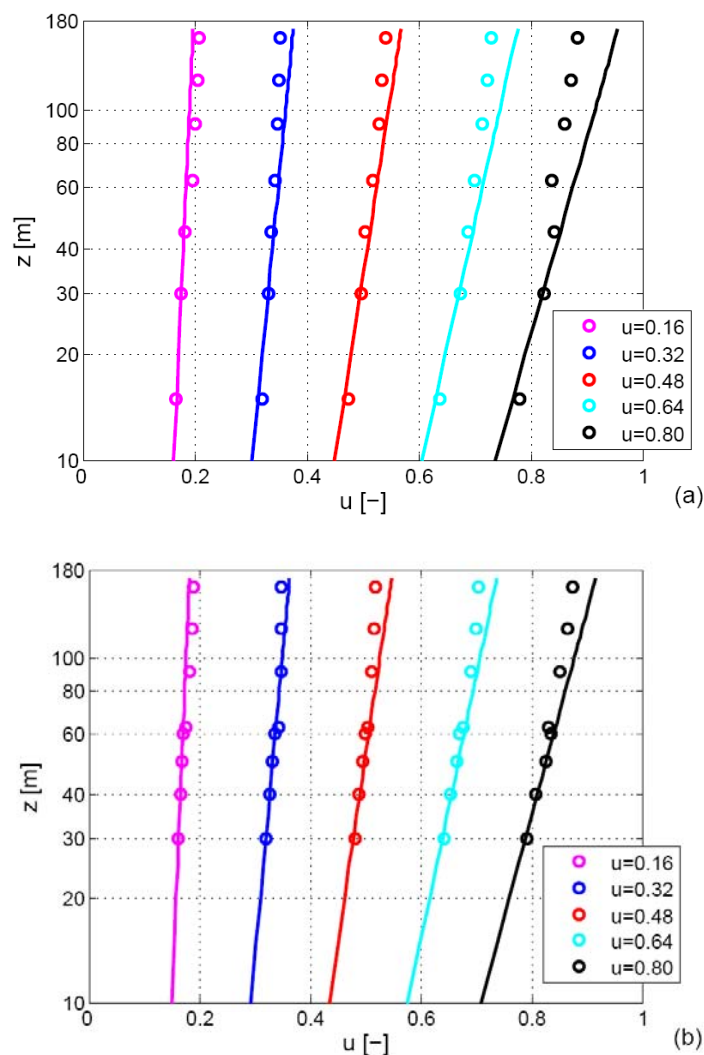


Figure 7.13. Comparison between the observations and the Charnock's wind profiles (solid lines) using the logarithmic profile. The wind speed is normalized with the highest observation value. (a) M2 and LiDAR. (b) M6 and LiDAR.

The figure shows that the prediction of wind speed performed by the logarithmic profile in combination with Charnock's relation is always good for the cup measurements which are in the surface layer. Greater deviations are found for the LiDAR profiles especially for the higher wind speeds. This may be due to the fact that over the platform, the LiDAR profiles are driven by a different roughness length. The value used for the Charnock's parameter is 0.012.

#### 7.2.4 Turbulence profiles

Using the different normalized mean wind speeds in Figure 7.13 and the results of the variation of turbulence intensity with normalized mean wind speed from Figure 7.7, different profiles of turbulence intensity can be derived for the highest four ranges of mean wind speed. The results were fitted with a model which accounts for the variation of turbulence intensity with height. The assumption in the model is that the turbulence is proportional in the surface layer to the friction velocity:

$$\sigma_u = Au_* \quad (7.5)$$

Thus by using Eq. (7.5) in combination with the logarithmic wind profile, Eq. (7.2) and the definition of the turbulence intensity, Eq (7.1), the variation of turbulence intensity is given by:

$$I_u = \frac{A\kappa}{\ln\left(\frac{z}{z_o}\right)} \quad (7.6)$$

The results are illustrated in Figure 7.14.

In Eq. (7.6), two parameters are unknown: the sea roughness length and the constant  $A$ . Therefore, with two observations of turbulence intensity at different levels, these parameters can be determined from a least squares fit. The lowest variation between the measurements and the model were found when the roughness length was estimated using Charnock's model, i.e. with the roughness length computed in Figure 7.13. As it is observed from Figure 7.14, the model predicts well the turbulence variation for the lowest wind speed range ( $u=0.32$ ) but it shows great variations for higher wind speed ranges for both masts. The value found for the constant  $A$  is around 2.5 for both masts on the medium wind speed ranges ( $u=0.48$ ,  $u=0.62$ ) but it increases for lower and higher ranges. The value of 2.5 is actually the one suggested in the Danish Standard (DS 472, 1992). In contrast, the LiDAR turbulence intensity profiles do not follow the mast profiles due to the effect of the attenuation already mentioned. Nevertheless, they follow the behavior of the cup profiles where the lowest turbulence intensities are found on the medium range of wind speeds as it was previously illustrated in Figure 7.7.

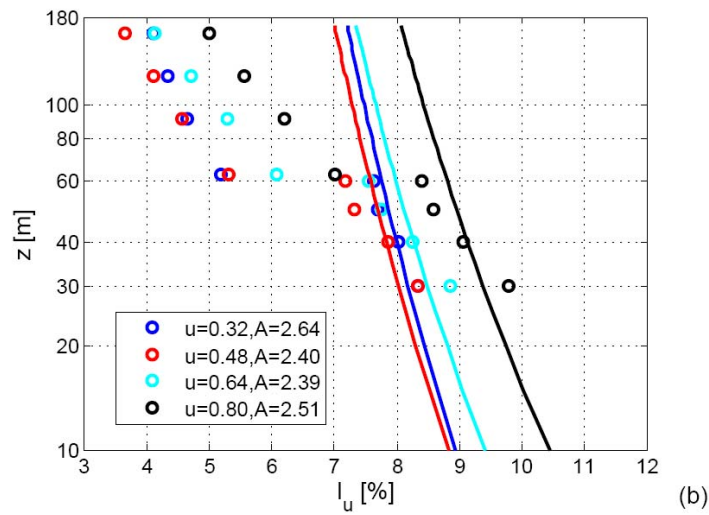
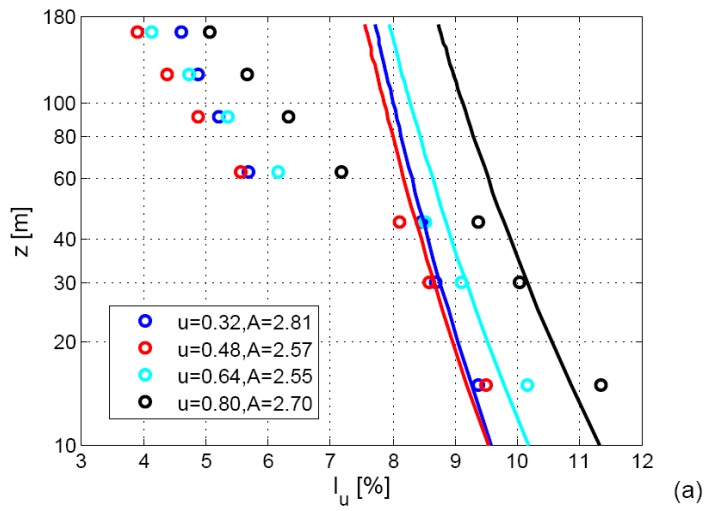


Figure 7.14. Turbulence intensity profiles for different wind speed ranges. The solid lines correspond to the model where the Charnock's relation was used for the roughness length. (a) M2 and LiDAR. (b). M6 and LiDAR.

## 8 Summary

The major objective of the 12MW project experimental campaign at the Horns Rev offshore wind farm in the North Sea was to collect observations of wind and turbulence from state-of-the-art remote sensing instruments. This was successfully accomplished by a close collaboration between DONG energy and Risø National Laboratory DTU. High-quality data were obtained from a 6-month experiment using the focused Doppler laser ZephIR wind SoDAR and the AQ500 SoDAR mounted 20 m above mean sea level on the transform platform. In parallel, meteorological observations from three tall masts, up to 70 m, were collected. The campaign took place from 3 May to 24 October 2006.

The report presents the experimental site and data collection. All data are stored in a database. The technical details on the LiDAR instrument and its operation during the campaign are provided as well as the theoretical background for turbulence and turbulent kinetic energy.

Based on the observations in the database, the analysis has been made. Firstly, comparison between the LiDAR and SoDAR wind observations showed good agreement. Secondly, comparison between LiDAR and cup anemometer wind observations from three masts showed good agreement. Thirdly, the cup anemometer data and LiDAR data were used to calculate wind profiles up to 160 m above mean sea level. The results are state-of-the-art and in reasonable agreement with theoretical description, e.g. the logarithmic wind profile, for an ensemble of all data (regardless of stability) for specific wind conditions, e.g. open sea (no fetch limitation).

For other wind direction sectors the influence of land and of the wind farm wake was clear in the profiles. For the wake, the maximum deficit observed at hub-height is 15%.

Also the turbulence observed from LiDAR and cup anemometers are compared with good results. In particular, LiDAR and cup anemometers both observe the decrease for winds up to  $10 \text{ ms}^{-1}$ , then increase due to the roughing of the sea as a function of wind speed. In agreement with the theory on turbulence observations using LiDAR, the findings from turbulence levels observed by LiDAR is somewhat lower than from cup anemometers at Horns Rev. A decrease in turbulence level as a function of height is clearly demonstrated from the analysis.

Further analysis is on-going on the effect of stability (observed by temperature sensors on the masts, from below the sea surface and from Sea Surface Temperature (SST) observed from satellite).

Observations from ceilometer at Christiansø in the Baltic Sea and from the North Atlantic Ocean reveal rather low mixing layer heights far offshore. This is relevant for understanding of the wind profile at higher levels, as the mixing layer height is an important scaling factor beyond the lower 10% of the boundary layer, the so-called surface boundary layer. In the study at Horns Rev, it appears that the surface boundary layer may not extend all the way to the 160 m observed during the experiment. Further investigation is in progress.

## **9 Conclusion and future work**

In the 12MW project an experimental campaign at the Horns Rev offshore wind farm was conducted in the period May to October 2006. This was done in cooperation between DONG energy and Risoe National Laboratory DTU. The observations from remote sensing technologies, LiDAR and SoDAR, are analyzed. In particular, the wind and turbulence observations from LiDAR provide new insight to wind profiles and turbulence levels at high levels in the atmosphere offshore, up to 161 m above sea level. Further analysis of the collected observations is in progress.

A new experiment in the 12MW project is planned at Høvsøre, Risø DTU in the winter 2007/2008 with the aim to observe wind and turbulence with LiDAR at even higher levels and to include detailed aerosol profiles observations as well as ceilometer and radiosoundings to infer the boundary layer height.

## **Acknowledgements**

Funding from The Danish Council for Strategic Research during the year 2006 to 2009, Sagsnr. 2104-05-0013 is greatly appreciated. Sea Surface Temperature (SST) maps from Jacob Høyer are appreciated.

## References:

- Antoniou, I., Jørgensen, H. E., Mikkelsen, T., Frandsen, S., Barthelmie, R., Perstrup, C. & Hurtig, M. Offshore wind profile measurements from remote sensing instruments. 1-10. 2006. Brussels, European Wind Energy Association. European Wind Energy Conference and Exhibition 2007, Athens.
- Antoniou, I., Jørgensen, H.E., Ormel, F., Bradley, S., Hünerbein, S.V., Emeis, S., Warmbier, G. 2003a On the theory of SODAR measurement techniques, Risø-R-1410, Roskilde, Denmark
- Antoniou, I.; Jørgensen, H.E., 2003b Comparing SODAR to cup anemometer measurements. In: Proceedings CD-ROM. CD 2. European wind energy conference and exhibition 2003 (EWEC 2003), Madrid (ES), 16-19 Jun 2003. (European Wind Energy Association, Brussels, 2003) 9 p
- Antoniou, I., Jørgensen, H.E., Hünerbein, S.v., Bradley, S.G., Kindler, D., 2004b, Inter-comparison of commercially available SODARs for wind energy applications. Proceedings of the 12th International Symposium on Acoustic Remote Sensing (ISARS) Conference, 11-16 July 2004, Cambridge, UK.
- Antoniou, I., Jørgensen, H.E., Mikkelsen, T., Pedersen, T.F., Warmbier, G., Smith, D. 2004a, Comparison of wind speed and power curve measurements using a cup anemometer, a LIDAR and a SODAR, In: Proceedings of the European Wind Energy Conference and Exhibition 2004 (EWEC 2004), London (UK), 22-25 Nov. 2004. 10 p.
- Barthelmie, R.J. 1999: The effects of atmospheric stability on coastal wind climates. *Meteorological Applications*, 6(1), 39-48.
- Barthelmie, R.J. 2001: Evaluating the impact of wind induced roughness change and tidal range on extrapolation of offshore vertical wind speed profiles. *Wind Energy*, 4(3), 99-105.
- Barthelmie, R.J. 2002: Modelling and measurements of coastal wind speeds. In: *Renewable Energy: Trends and Prospects*, Pennsylvania Academy of Sciences, Easton, PA, pp. 161-175.
- Barthelmie, R.J., Folkerts, L., Ormel, F.T., Sanderhoff, P., Eecen, P.J., Stobbe, O. and Nielsen, M. 2003: Offshore wind turbine wakes measured by SODAR, *Journal of Atmospheric and Oceanic Technology*, 30(4), 466-477.
- Batchvarova, E. & Gryning, S. E. (2006). Progress in urban dispersion studies. *Theoretical and Applied Climatology*, 84, 57-67.
- Businger, J., Wyngaert, J., Izumi, Y., and Bradley, E. 1971: Flux-profile relationships in the atmospheric surface layer, *J. Atmos. Sci.*, 28, 181-189.
- Charnock, H., 1955: Wind stress over a water surface, *Q. J. R. Meteorol. Soc.*, 81, 639-640.
- de Vries, E. (2005). Thinking bigger: Are there limits to turbine size? *Renewable Energy World*, May-June 2005. 42-55
- DS 472, 1992, Code of practice for loads and safety of wind turbine constructions.' DS 472, The Danish Society of Engineers and the Federation of Engineers

- Elsam Engineering, 2005, Skyggevirkning efter Horns Rev Havmøllepark. Meteorologisk målesystem og måledata, M6 & M7. Report Nr. 13983. Elkraft System, PSO - F&U 2002 / FU2103. Eltra no. 4158. ELSAM-VU111.
- Gryning, S.-E.; Holtslag, A.A.M.; Irwin, J.S.; Sivertsen, B., Applied Dispersion Modelling Based on Meteorological Scaling Parameters. *Atmos. Environ.* (1987) v. 21 p. 79-89
- Gryning, S-E and Batchvarova, E. 2002 Marine boundary layer and turbulent fluxes over the Baltic Sea: measurements and modelling. *Boundary-layer meteorology* 103: 29-47.
- Gryning, S-E. Batchvarova, E., Brümmer, H., Jørgensen, H., and Larsen, S.. On the extension of the wind profile over homogeneous terrain beyond the surface layer. *Boundary-Layer Meteorol.*, 124:251–268, 2007.
- Gryning, S.-E.; Batchvarova, E., A model for the height of the internal boundary layer over an area with a irregular coastline. *Boundary-Layer Meteorol.* (1996) 78 , 405-413
- Gryning, S.-E.; Batchvarova, E., Marine atmospheric boundary-layer height estimated from NWP model output. *Int. J. Environ. Pollut.* (2003) 20 , 147-153
- Hara, T., Belcher, S. 2004 Wind profile and drag coefficient over mature ocean surface wave spectra. *J. Phys. Oceanogr.* 34:2345–2358.
- Hasager, C.B., Dellwik, E., Nielsen, M. and Furevik, B. 2004 Validation of ERS-2 SAR offshore wind-speed maps in the North Sea. *Int. J. Remote Sensing*, vol 2, 19, p. 3817-3841
- Högström, U., Smedman, A.S., Bergström, H. 2006. Calculation of wind speed variation with height over the sea. *Wind Engineering* 30:269–286
- Høyer, J. L. & She, J. (2007). Optimal interpolation of sea surface temperature for the North Sea and Baltic Sea. *J.Mar.Sys.*, 65, 176-189.
- IEC 61400-12-1, 2005, Wind turbines – Part 12-1:Power performance measurements of electricity producing wind turbines. Int. Electrotechnical Commission.
- Jensen, L.E., C. Mørch, P. B. Sørensen, K. H. Svendsen. 2004 Wake measurements from the Horns Rev wind farm. European Wind Energy Conference and Exhibition, London 2004. p.1-9.
- Jørgensen, H.E.; Mikkelsen, T.; Streicher, J.; Herrmann, H.; Werner, C.; Lyck, E., LiDAR calibration experiments. *Appl. Phys. B* (1997) 64 , 355-361
- Jørgensen, H.E.; Mikkelsen, T., Effects of averaging LiDAR signals. In: Improvement of LiDAR measurement techniques for discrimination of polar stratospheric clouds and volcanic aerosols. Final report. Werner, C. (ed.), (DLR. Institute of Optoelectrics, Wessling (DE), 1995) 11 p.
- Kaimal, J.C., Finnigan, J.J. 1994, Atmospheric boundary layer flows. Their structure and measurement, Oxford, Oxford University Press.
- Kamp, L. M., 2004, Wind turbine development 1973-2000: A critique of the differences in policies between the Netherlands and Denmark: *Wind Engineering*, v. 28, no. 4, p. 342-354
- Kraus, E.B., 1972 Atmosphere-Ocean interaction. Oxford University Press.
- Lange, B.; Larsen, S.E.; Højstrup, J.; Barthelmie, R.J., 2004 The influence of thermal effects on the wind speed profile of the coastal marine boundary layer. *Boundary-Layer Meteorol.* 112 , 587-617'

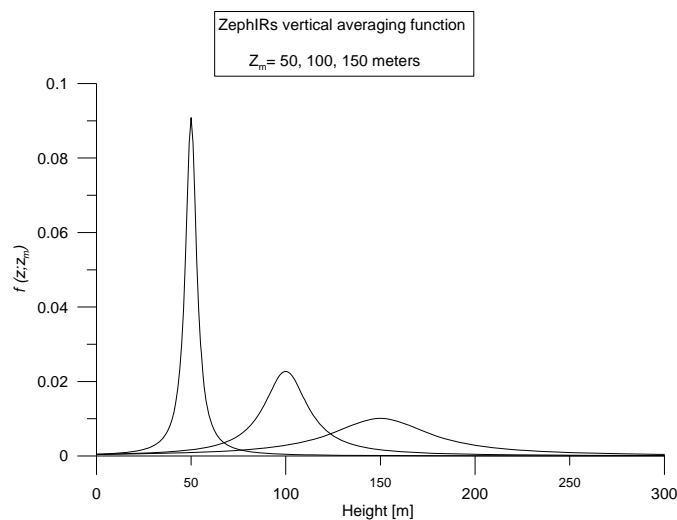
- Larsén, X.G. 2003. Air-sea exchange of momentum and sensible heat over the Baltic Sea. Acta Universitatis Upsaliensis, Comprehensive summaries of Uppsala Dissertations from the Faculty of Science and Technology 820, ISBN 91-554-5565-4. Uppsala.
- Pedersen, T.F., 2004 Characterisation and classification of Risø P2546 cup anemometer., Risø-R-1364, Roskilde, Denmark
- Peña, A., Hasager, C. B., Gryning, S. E., Courtney, M., Antoniou, I. & Mikkelsen, T. (2007). Offshore wind profiling using LiDAR measurements. Wind Energy, in review
- Perrin, D, McMahon N., Crane, M., Ruskin., H.J., Crane., L., Hurley, B., 2007: The effect of a meteorological tower on its top-mounted anemometer. Applied Energy, 84, 413-424.
- Pryor, S.C. and Barthelmie, R.J. 2002: Statistical analysis of flow characteristics in the coastal zone. Journal of Wind engineering and Industrial Aerodynamics, 90, 201-221
- Smedman AS, Hogstrom U, Hunt JCR 2004 Effects of shear sheltering in a stable atmospheric boundary layer with strong shear. Quarterly J. Royal Meteorological Society 130 (596): 31-50 Part A JAN 2004
- Smedman AS, Bergstrom H, Hogstrom U Spectra, variances and length scales in a marine stable boundary layer dominated by a low level jet. Boundary-Layer Meteorology 76 (3): 211-232 NOV 1995
- Smedman, A.S., Larsén, X.G., Högström, U., Kahma, K., Peterson, H. 2003. Effect of the sea state on the momentum exchange over the sea during neutral conditions. J. Geophys. Res. 108 (C11), 3367, doi:10.1029/2002JC001526
- Smith, D. A., Harris, M., Coffey, A. S., Mikkelsen, T., Jørgensen, H. E., Mann, J. & Danielian, G. (2007). Wind lidar evaluation at the Danish wind test site in Høvsøre. Wind Energy, 9, 87-93.
- Sommer,A. Offshore measurements of wind and waves at Horns Rev and Laesoe, Denmark. 65-79. 2003. Athena. OWEMES Conference Proceedings, 10-12 April 2003, Naples, Italy.
- Stoffelen, A., and Anderson, D., 1997, Scatterometer data interpretation: Estimation and validation of the transfer function CMOD4. Journal of Geophysical Research, 102, C3, 5767-5780.
- Sørensen, J. H., Sensitivity of the DERMA Long-Range Gaussian Dispersion Model to Meteorological Input and Diffusion Parameters. Atmos. Environ.,(1998) 24, 4195-4206.
- Sørensen,PB. 2005a, Wake effect east of the Horns Rev offshore wind farm. Technical description of meteorological measurement system. Elsam No. VU 111, Eltra no. 4158, Elkraft System, PSO- F&U 2002/FU2103.
- Sørensen,PB. 2005b, Wake effect east of the Horns Rev offshore wind farm. Presentation of meteorological measurements Aug 2003 – Nov 2004. Elsam No. VU 111, Eltra no. 4158, Elkraft System, PSO- F&U 2002/FU2103.
- Vogelezang, D. and Holtslag, A., Evaluation and Model Impacts of Alternative Boundary-Layer Height Formulations. Boundary-Layer Meteorol.,(1996) 81, 245-269.

## Appendix I

Mathematica filter evaluation program: LiDARfilter\_HEJ\_TM\_04.nb

The width  $z_R$  increases with the LiDAR's measurement range  $L$  to the second power, and can to a good approximation for the QQ ZephIR LiDAR be parameterized as 6:

$$z_R(L) \approx 0.00085 L^2 [m] \quad (4.21)$$




---

6

Mike Harris, in his chapter in the UPWIND (2006) progress report, states that the QQLiDARs Half-Width\_Half\_maximum (HWHM) at range 100 meters is: 8.5 meters). This is in agreement with the calculations in the QQ LiDAR table <sup>TM</sup>.

Setting the ZephIR's measurement height to 100 meters, the optical systems focal length  $R$  (with the fixed 30 degrees wedge) is 115.47 meters, and the corresponding "HWHM" parameter  $z_R$  is  $8.5 \cdot (115.47/100)^2 \sim 11.3$  m. Full Width at Half maximum for ZephIR measurements at height 100 m is therefore 22.68 m. This measurement volumes projection on a horizontal plane is  $22.68 \sin(30) \sim 11.34$  m.

Risø's research is aimed at solving concrete problems in the society.

Research targets are set through continuous dialogue with business, the political system and researchers.

The effects of our research are sustainable energy supply and new technology for the health sector.

